Geophysical Journal International

Geophys. J. Int. (2022) **230,** 507–527 https://doi.org/10.1093/gji/ggac055
Advance Access publication 2022 February 09
GJI Seismology

Constraining deep mantle anisotropy with shear wave splitting measurements: challenges and new measurement strategies

Jonathan Wolf,[1] Maureen D. Long,[1] Kuangdai Leng[2,3] and Tarje Nissen-Meyer[2]

[1]*Department of Earth and Planetary Sciences, Yale University, New Haven, CT 06520, USA. E-mail: jonathan.wolf@yale.edu*
[2]*Department of Earth Sciences, University of Oxford, Oxford OX1 3AN, United Kingdom*
[3]*Rutherford Appleton Laboratory, Harwell Campus, Didcot OX11 0QX, United Kingdom*

Accepted 2022 February 5. Received 2022 January 13; in original form 2021 October 18

SUMMARY

Determinations of seismic anisotropy, or the dependence of seismic wave velocities on the polarization or propagation direction of the wave, can allow for inferences on the style of deformation and the patterns of flow in the Earth's interior. While it is relatively straightforward to resolve seismic anisotropy in the uppermost mantle directly beneath a seismic station, measurements of deep mantle anisotropy are more challenging. This is due in large part to the fact that measurements of anisotropy in the deep mantle are typically blurred by the potential influence of upper mantle and/or crustal anisotropy beneath a seismic station. Several shear wave splitting techniques are commonly used that attempt resolve seismic anisotropy in deep mantle by considering the presence of multiple anisotropic layers along a raypath. Examples include source-side *S*-wave splitting, which is used to characterize anisotropy in the deep upper mantle and mantle transition zone beneath subduction zones, and differential S-ScS and differential SKS-SKKS splitting, which are used to study anisotropy in the D'' layer at the base of the mantle. Each of these methods has a series of assumptions built into them that allow for the consideration of multiple regions of anisotropy. In this work, we systematically assess the accuracy of these assumptions. To do this, we conduct global wavefield modelling using the spectral element solver AxiSEM3D. We compute synthetic seismograms for earth models that include seismic anisotropy at the periods relevant for shear wave splitting measurements (down to 5 s). We apply shear wave splitting algorithms to our synthetic seismograms and analyse whether the assumptions that underpin common measurement techniques are adequate, and whether these techniques can correctly resolve the anisotropy incorporated in our models. Our simulations reveal some inaccuracies and limitations of reliability in various methods. Specifically, explicit corrections for upper mantle anisotropy, which are often used in source-side direct *S* splitting and S-ScS differential splitting, are typically reliable for the fast polarization direction ϕ but not always for the time lag δt, and their accuracy depends on the details of the upper mantle elastic tensor. We find that several of the assumptions that underpin the S-ScS differential splitting technique are inaccurate under certain conditions, and we suggest modifications to traditional S-ScS differential splitting approaches that lead to improved reliability. We investigate the reliability of differential SKS-SKKS splitting intensity measurements as an indicator for lowermost mantle anisotropy and find that the assumptions built into the splitting intensity formula can break down for strong splitting cases. We suggest some guidelines to ensure the accuracy of SKS-SKKS splitting intensity comparisons that are often used to infer lowermost mantle anisotropy. Finally, we suggest a new strategy to detect lowermost mantle anisotropy which does not rely on explicit upper mantle corrections and use this method to analyse the lowermost mantle beneath east Asia.

Key words: Numerical modelling; Planetary interiors; Computational seismology; Seismic anisotropy; Wave propagation.

1 INTRODUCTION

Seismic anisotropy is defined as the dependence of seismic wave speeds on the propagation or polarization direction of the wave. Seismic anisotropy is almost absent in the bulk of the lower mantle (e.g., Panning & Romanowicz 2006), but it has been detected in the crust (e.g., Barruol & Kern 1996; Erdman *et al.* 2013), the upper mantle (e.g., Silver 1996; Chang *et al.* 2014) and the mantle transition zone (e.g., Yuan & Beghein 2014; Chang & Ferreira 2019). There are also some indications that anisotropy might be present in the uppermost part of the lower mantle beneath subduction systems (e.g., Foley & Long 2011; Lynner & Long 2015; Mohiuddin *et al.* 2015; Chang & Ferreira 2019; Ferreira *et al.* 2019). Furthermore, the lowermost 200–300 km of the mantle, referred to as the D'' layer, has been found to display seismic anisotropy (e.g., Garnero *et al.* 2004; Wookey *et al.* 2005; Nowacki *et al.* 2010; Creasy *et al.* 2017; Wolf *et al.* 2019; Lutz *et al.* 2020). An accurate and complete characterization of lowermost mantle anisotropic geometry, however, is difficult to achieve, partly due to limited geographical and backazimuthal sampling, noisy data and/or the limits of methods used to detect seismic anisotropy (e.g., Creasy *et al.* 2017). A thorough understanding of lowermost mantle anisotropy is important, however, to resolve the deformation geometry and thus plausible directions of mantle flow (e.g., Long & Becker 2010).

The study of deep mantle anisotropy has potential to shed light on several interesting scientific problems. In the transition zone and uppermost lower mantle, anisotropy may provide clues to the deformation associated with subducting slabs impinging on the higher-viscosity lower mantle and to the patterns of mantle flow in the deep portions of subduction systems. In the lowermost mantle, anisotropy may reveal flow patterns at the base of the mantle, which may in turn shed light on the origin and dynamics of enigmatic structures. For example, the precise nature of two large-scale antipodal regions with reduced shear wave velocities—the so-called large-low shear velocity provinces (LLSVPs)—is still poorly understood (e.g., Dziewonski *et al.* 2010; Wolf & Evans 2022). They may be primarily caused by temperature effects (e.g., Wang & Wen 2004), but they have also been suggested to be compositionally distinct (e.g., Davaille & Romanowicz 2020). D'' anisotropy has often been found at LLSVP edges (e.g., Creasy *et al.* 2017; Reiss *et al.* 2019; Cottaar & Romanowicz 2013); the precise nature and geometry of this anisotropy may shed light on the characteristics of LLSVPs.

A major challenge for the study of anisotropy in the deep mantle is uncertainty regarding the precise mechanism causing anisotropy. For the mid-mantle, lattice preferred orientation (LPO) of wadsleyite and bridgmanite might explain measurements of seismic anisotropy, while ringwoodite and garnet are nearly isotropic (e.g., Faccenda 2014). For D'' anisotropy, a likely scenario is deformation-induced LPO of bridgmanite (Br), post-perovsikte (Ppv) or ferropericlase (Fp; Nowacki *et al.* 2011). Precise measurements of the anisotropic geometry in the lowermost mantle may be able to distinguish the presence of these different minerals (e.g., Creasy *et al.* 2017; Wolf *et al.* 2019). Furthermore, better knowledge of mineralogy and deformation in the lowermost mantle can give insights about the heat flow (e.g., Hernlund *et al.* 2005) across the core–mantle boundary (CMB) that is driving mantle convection.

Anisotropy in Earth's upper mantle is more straightforward to measure than anisotropy in the deep mantle. The reasons for this include the better raypath coverage for upper mantle applications, and also the greater methodological flexibility. Besides shear wave splitting, receiver function analysis (e.g., Levin & Park 1997; Schulte-Pelkum *et al.* 2005; Nikulin *et al.* 2009; Wirth & Long 2012) or surface wave tomography (e.g., Panning & Nolet 2008; Ferreira *et al.* 2010; Fry *et al.* 2010) can reveal information about upper mantle (and crustal) anisotropy, but neither technique is applicable to the lowermost mantle (although surface wave studies can provide some resolution of the transition zone and uppermost lower mantle, particularly when overtone data is included; for example Yuan & Beghein 2014). Tomographic approaches have also been used to map radial anisotropy throughout the mantle (e.g., Panning & Romanowicz 2006), including the D'' region. However, estimates of lowermost mantle radial anisotropy may be affected by tradeoffs between isotropic and anisotropic structure (e.g., Kustowski *et al.* 2008; Chang *et al.* 2015). A complimentary approach to resolving deep mantle anisotropy, studies mostly relies on body waves, specifically measurements of shear wave splitting. An inherent challenge with these techniques is that shear waves accumulate their anisotropic signature along the whole raypath. Therefore, isolating the influence of the deep mantle, and correcting for splitting accrued in the upper mantle, is crucial. The dilemma basically reduces to the problem of extracting information from a seismic wave that travels through multiple anisotropic layers. Generally, this can be done in two different ways. First, an integrated measurement can be corrected for the influence of certain layers along the raypath if their anisotropy is known. A secondly, closely related, approach is to compare phases that have a very similar raypath through one anisotropic layer. Differences in the anisotropic signature can be attributed to those parts of the Earth where the raypaths of the phases in question are separated.

A variety of different seismic phases and methodological approaches are used to characterize anisotropy in the deep mantle. For the transition zone and uppermost lower mantle, so-called source-side splitting of direct teleseismic *S* phases is a common approach to characterize anisotropy near the earthquake source (Russo & Silver 1994; Lynner & Long 2013; Walpole *et al.* 2017; Eakin *et al.* 2018). In this approach, the upper mantle anisotropy beneath the receiver is characterized using SKS waves, ideally over a wide range of backazimuths, and this information is used to correct direct *S* waves for the effect of upper mantle splitting before the source-side contribution is measured. For the lowermost mantle, a common measurement strategy relies on S-ScS differential splitting to infer the geometry of the anisotropy (e.g., Wookey *et al.* 2005; Nowacki *et al.* 2010; Creasy *et al.* 2017; Wolf *et al.* 2019). This method is based upon several assumptions. First, as with the source-side direct *S* splitting method, the seismograms are corrected for the anisotropic contribution in the upper mantle/crust on the receiver side. The accuracy of these corrections have not, to our knowledge, been validated against full-wave simulations so far. Secondly, the assumption is made that S and ScS phases have a similar sensitivity in the receiver side upper mantle, so that ScS splitting in the source side upper mantle can be inferred by measuring splitting of the *S* phase. Again, this assumption has not been thoroughly tested so far in the context of global wavefield simulations. One aspect that has been tested is how well ray theory can predict the lowermost mantle splitting of ScS in absence of upper mantle anisotropy. Nowacki & Wookey (2016) showed that full-wave effects can be large for complex anisotropic scenarios, while the results from Wolf *et al.* (2022) suggest that for a uniformly anisotropic lowermost mantle, ray theory can predict the D'' splitting well. Another potential concern is distortion of the radial and transverse components due to isotropic structure which could potentially mimic splitting for some phases at certain distance ranges (Parisi *et al.* 2018).

SKS-SKKS differential splitting is a similarly popular method to detect seismic anisotropy in the lowermost mantle (e.g., Niu & Perez 2004; Deng *et al.* 2017; Grund & Ritter 2018; Reiss *et al.* 2019; Wolf *et al.* 2019; Lutz *et al.* 2020; Asplet *et al.* 2020). Tesoniero *et al.* (2020) used global wavefield simulations to show that models with lowermost mantle anisotropy do predict SKS-SKKS differential splitting, as expected from ray theory; they further showed that only relatively large differences in splitting intensity of SKS and SKKS phases should be interpreted as reflecting a lowermost mantle anisotropy contribution. However, Tesoniero *et al.* (2020) only used relatively weak anisotropy in their simulations, and did not thoroughly examine the assumptions made by the SKS-SKKS differential splitting measurement technique for a range of anisotropy models.

The goal of this work is to thoroughly examine and evaluate the various assumptions made in commonly used frameworks to measure anisotropy in the deep mantle (source-side direct *S* splitting, differential S-ScS splitting and SKS-SKKS splitting intensity discrepancy measurements). We do this in the context of global wavefield simulations, building upon previous work by Tesoniero *et al.* (2020) and Wolf *et al.* (2022), who have established the spectral element solver AxiSEM3D (Leng *et al.* 2016, 2019) as a viable tool to examine finite-frequency effects on measurements of shear wave splitting. Tesoniero *et al.* (2020) previously investigated full-wave effects on differential SKS-SKKS splitting measurements for a limited suite of anisotropic models. We expand on these results here, with the goal of evaluating the assumptions built into the differential SKS-SKKS splitting intensity method. Specifically, we examine the influence of anisotropy strength on the reliability of differential SKS-SKKS splitting intensities, because measurements of splitting intensity make some fairly restrictive assumptions about the strength of anisotropy. Next, we systematically analyse the accuracy of explicit corrections for the influence of multiple anisotropic layers, which are based on ray theory. We do this by investigating how well an explicit anisotropy correction for a single upper mantle anisotropic layer works for a range of anisotropic geometries and symmetry classes, including various types of olivine fabric and exploring the implications of our simulations for both source-side direct *S* splitting measurements and S-ScS differential splitting.

We next analyse the full set of assumptions built into the S-ScS differential splitting technique in detail. In previous work, the raypath of ScS in the lowermost mantle was often assumed to be horizontal (Wookey *et al.* 2005; Ford *et al.* 2015; Creasy *et al.* 2017; Wolf *et al.* 2019), which has been shown to be an oversimplification in many circumstances (Nowacki & Wookey 2016; Wolf *et al.* 2022). Due to this common assumption, the effects of the reflection of the ScS phase off the CMB are not typically been considered in detail. We explore these effects through a series of wavefield simulations, and show that a version of the method that explicitly takes into account the effect of the CMB reflection works reliably in many cases (particularly when the anisotropic contribution of the upper mantle is not too strong). Building upon these results, we suggest a new strategy for detecting seismic anisotropy in the lowermost mantle that compares the *S* and ScS waveforms that are rotated into a radial-transverse coordinate frame. We use this S-ScS waveform comparison technique to interrogate the anisotropic structure of the lowermost mantle beneath east Asia. While only some of the phases we examine show convincing evidence for anisotropy, we do resolve some small-scale gradients in (an-)isotropic behaviour.

2 METHODS

2.1 Computation of synthetic seismograms

We conduct 3-D global wavefield simulations using the coupled spectral element solver AxiSEM3D (Leng *et al.* 2016, 2019). Due to its computational efficiency, AxiSEM3D allows us to compute synthetic seismograms for periods relevant for shear wave splitting (down to 5 s). The use of the anisotropic module implemented by Tesoniero *et al.* (2020) makes it possible to compute seismograms for arbitrary anisotropy incorporated in the different input models. In this work, we either incorporate global layers of seismic anisotropy into our models, or (for models that include heterogeneity in anisotropy) we specify large enough regions of seismic anisotropy that transitional effects at boundaries between different domains do not affect the splitting behaviour (Wolf *et al.* 2022). Our models incorporate layer(s) of seismic anisotropy in the upper mantle, the lowermost mantle, or both. Based on the expected splitting behaviour for different models as determined by ray theory, which underpins the set of assumptions made in the shear wave splitting methods we evaluate, we can determine the accuracy of the methods by measuring splitting from the synthetic seismograms.

The setup for many of the our simulations is shown in Fig. 1. We conveniently place our station at the north pole and then simulate earthquakes at an epicentral distance of 60° for ScS phases and a distance of 120° for SK(K)S phases. At these distances and source depths, no contamination of S-ScS and SK(K)S from other phases is expected (Wolf *et al.* 2022). We simulate earthquakes at 0 km depth for our initial set-up to be certain we avoid any contamination from surface reflections (depth phases). Subsequently, we also investigate deeper earthquakes (500 km depth), again making sure that no depth phases contaminate the arrivals at the chosen distances. For our initial model setup, the focal mechanism is chosen to lead to an *S* wave that is radially polarized (before undergoing splitting), with M_{tt} as the only non-zero component of the moment tensor. For SK(K)S phases, which are always fully SV polarized due to *P*-SV coupling at the CMB, this approach yields large amplitudes in the synthetic seismograms. Our precise knowledge of the initial polarization of *S* and ScS phases facilitates the validation of the S-ScS differential splitting method, for which the correct determination of the initial polarization plays a crucial role. Apart from the question of the initial *S*-wave polarization, the details of the focal mechanism are generally unimportant for this study. Whenever necessary, we will systematically move away from the starting setup shown in Fig. 1; for example, we adjust epicentral distances and initial polarizations for some of our simulations. These departures from our base set-up will always be explicitly mentioned in the corresponding parts of the paper.

2.2 Implementation of anisotropic models

The background velocity structure in our simulations is always isotropic PREM (Dziewonski & Anderson 1981). We use two types of input models to overwrite the PREM velocity structure at certain depths: the first type specifies an anisotropic layer in the upper mantle (source and/or receiver side), and the other does the same in the lowermost mantle. In both cases, a typical layer thickness in our input models would be ∼150 km, although modifications to the layer thickness are made to change the magnitude of splitting. We modify the strength of splitting in our simulations by adjusting layer thickness instead of anisotropic strength. Therefore, we avoid

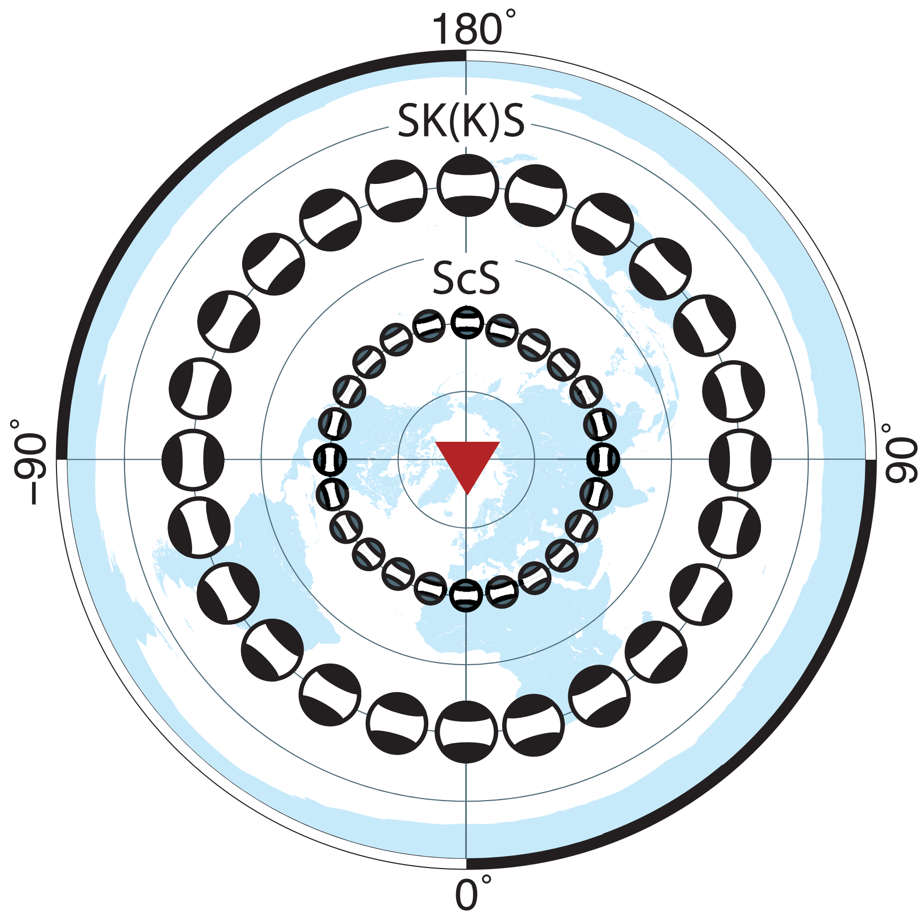

Figure 1. Schematic representation of a typical source–receiver configuration in our numerical modelling. The epicentral distance from source to receiver is 120° for SK(K)S and 60° for ScS phases. Focal mechanism diagrams represent the sources, placed every 15°, the red triangle at the north pole represents the station. For the moment tensors the only non-zero component is M_{tt}.

having to manipulate the experimentally derived elastic tensors that are used in this study. A functionally equivalent approach would be to mix the tensors with their isotropic equivalents to increase or decrease the the strength of anisotropy. In each simulation, the layers are either global or have a large enough extent that no full-waveform effects from their edges need to be taken into account (more details in Wolf *et al.* 2022). We use the full elastic tensor to specify the seismic anisotropy in our models. For the upper mantle, we either use a model of with horizontal transverse isotropy (HTI) symmetry, based on the characteristics of anisotropic PREM in the upper mantle but with the anisotropy rotated from vertical transverse isotropy (VTI) to HTI, or we use the olivine elastic tensors from Karato *et al.* (2008, table 21.1), assuming a horizontal simple shear configuration. In this paper, we mostly present results for HTI, along with olivine A-type and C-type; results for olivine E-type are presented in the Supporting Information. Our choice of an HTI elastic tensor allows us to investigate the behaviour of the transversely isotropic case in addition to more realistic tensors. While the precise precise details of the HTI elastic tensor are not important, our choice of this particular tensor allows us to build directly on previous work that has used it to model wavefield effects due to upper mantle anisotropy (Tesoniero *et al.* 2020). We do not focus on olivine B- and D-type because these fabric types would primarily be expected at relatively shallow depths (Karato *et al.* 2008) and in specific tectonic settings (for example, the ‘cold nose’ of the subduction zone mantle wedge; Kneller *et al.* 2005) and are found to require an unrealistically thick layer to lead to robust splitting.

For the lowermost mantle, we use elastic tensors calculated using viscoplastic self-consistent simulations from Creasy *et al.* (2020), particularly for post-perovskite (Ppv) and bridgmanite (Br). We mostly present results for a Ppv lowermost mantle in the main paper and in the Supporting Information we illustrate that our results are generally independent of the details of the elastic tensor, repeating some simulations with a Br-dominated lowermost mantle. While achieving robust upper mantle splitting in our simulations is relatively easy, the quality of lowermost mantle splitting measurements strongly depends on the precise direction from which the tensor is sampled (Wolf *et al.* 2022). To make sure our results are not distorted by large uncertainties in the lowermost mantle associated splitting parameters, the elastic tensor incorporated in D'' is rotated to a direction for which splitting measurements are found to be robust (following Wolf *et al.* 2022) and thus always sampled from the same direction. The sampling direction is then kept irrespective of backazimuth. For the upper mantle anisotropy, on the other hand, the direction from which the elastic tensor is being sampled will depend on the backazimuth. This convention is also useful because we will generally focus on corrections for upper mantle anisotropy for different anisotropic scenarios and sampling directions. By systematically rotating the lowermost mantle elastic tensors and thus keeping the splitting due to lowermost mantle anisotropy the same, these results can directly be compared with each other.

2.3 Shear wave splitting measurements

When a linearly polarized *S* wave enters an anisotropic medium, it splits into slow and fast quasi-*S* waves (e.g., Vinnik *et al.* 1989; Silver & Chan 1991). Splitting can be described by the time lag between the fast and the slow travelling wave (δt) and the polarization of the fast travelling *S* wave (ϕ), measured clockwise from the north. There are various strategies for measuring these parameters from teleseismic shear wave data (e.g., Bowman & Ando 1987; Silver & Chan 1991). Alternatively, or in addition, measurements of splitting intensity (*SI*, Chevrot 2000) can be used. *SI* relies on the similarity in waveform shapes between the transverse component and the time derivative of the radial components and can thus indicate the presence or absence of splitting along a raypath. *SI* is defined by

$$SI = -2\frac{T(t)R'(t)}{|R'(t)|^2} \approx \delta t \sin(2(\alpha - \phi)) , \qquad (1)$$

where $T(t)$ denotes the transverse component, $R^{'}(t)$ the radial component derivative and α the polarization of the incoming wave. For a single layer of anisotropy, this means that we can retrieve ϕ and δt from the phase and the amplitude of a $\sin 2\theta$ curve fit to the *SI* data as a function of initial polarization. The *SI* measurement is based on the assumption that the radial component can be expressed in terms of the incoming wavelet $w(t)$ as $R(t) \approx w(t)$ and the transverse as $T(t) \approx -\frac{1}{2}\delta t(\sin(2\alpha))w'(t)$, which is valid under the assumption that the time delay δt is small compared to the dominant period of the signal (Vinnik *et al.* 1989; Silver & Chan 1991; Chevrot 2000). This implies that the transverse component has the shape of the radial time derivative; again, this should be valid if splitting is not too strong. We will investigate the limits of this assumption for cases with large delay times in Section 3.3.

Before measuring splitting, we pre-process our synthetic data by applying a bandpass filter retaining energy between 6 and 25 s. For SK(K)S phases, we carry out all our splitting measurements using SplitRacer (Reiss & Rümpker 2017), a graphical user interface implemented into MATLAB. SplitRacer uses the transverse energy minimization technique (Silver & Chan 1991) to estimate the splitting parameters ϕ and δt, making use of the corrected error determination by Walsh *et al.* (2013). An updated version of the code (Reiss *et al.* 2019) also measures the splitting intensity, and we make splitting intensity measurements on our synthetic data as well. We have modified SplitRacer to account for arbitrary initial polarizations of *S* and ScS phases, using a pre-existing routine aimed at calculating the station misalignment from SK(K)S measurements. For cases in which no explicit anisotropy correction needs to be applied (that is, when measuring ScS splitting in the absence of upper mantle anisotropy), we use the SplitRacer code for the splitting measurements. For cases in which an explicit correction for upper mantle anisotropy is needed, we use an additional function that automatically processes (manipulated) SplitRacer output files. This additional function uses the eigenvalue minimization method (Silver & Chan 1991) to measure splitting. Specifically, for the case in which source side anisotropy corrections need to be applied (i.e., for source-side *S* and S-ScS differential splitting), we measure the source side splitting parameters from the *S* phase with SplitRacer. Then, the additional function uses the splitting parameters to correct the ScS waveforms and determine the lowermost mantle associated splitting parameters by minimizing the second eigenvalue of the covariance matrix (Silver & Chan 1991), building upon an implementation from Creasy *et al.* (2017). S-ScS differential splitting (Wookey *et al.* 2005), for which these source side corrections need to be applied, will be explained in detail in Section 2.4.

2.4 Overview of measurement strategies for deep mantle anisotropy

Because investigations of deep mantle anisotropy necessarily involve consideration of potential contributions to splitting from anisotropy in the upper mantle (and possibly the crust), it is necessary to develop strategies to account and/or correct for such shallow contributions. Put differently, isolating the deep mantle contribution to splitting involves extracting information about anisotropy in the (possible) presence of multiple anisotropic layers. Two different, but related, measurement strategies are commonly used. One strategy relies on the explicit correction of waveforms for the contribution of individual anisotropic layers along an integrated raypath is explicitly corrected for. For example, when splitting due to upper mantle anisotropy on the receiver side influencing an *S* phase is known, the waveforms can be corrected (through appropriate rotation and time-shifting of the components) for this contribution to isolate splitting due to upper mantle anisotropy at the source side (Fig. 2b). This technique is known as source-side splitting and is commonly used to study anisotropy beneath subducting slabs (e.g., Russo & Silver 1994; Russo *et al.* 2010; Lynner & Long 2014; Eakin & Long 2013). A more complicated procedure falling in this category would be S-ScS differential splitting (Fig. 2b; Wookey *et al.* 2005), in which contributions from the source side, the lowermost mantle, and the receiver side are considered separately, as explained in more detail below. A second strategy involves comparisons of different phases with similar raypaths in certain parts of the Earth, but different raypaths in the region of interest. If significant differential splitting signatures are found, then there must be a contribution from the part of the raypaths where the phases diverge substantially. An example is the SKS-SKKS differential splitting method (Fig. 2d). The raypaths of SKS and SKKS are very similar in the upper mantle, so large differences in splitting intensity are generally attributed to the lowermost mantle (e.g., Niu & Perez 2004; Long 2009; Tesoniero *et al.* 2020).

For measurements that rely on explicit corrections for anisotropy in the upper mantle (and crust) directly beneath the receiver, thorough knowledge of the splitting signature due to the upper mantle is necessary. Single-station average splitting parameters are sometimes used for such corrections, often relying on global SKS splitting databases (e.g., Barruol *et al.* 2009). Some authors have argued that only stations that overlie relatively simple, or particularly weak, upper mantle anisotropy should be used for studies that rely on explicit receiver-side corrections (e.g., Lynner & Long 2013, 2014). If relatively simple upper mantle anisotropy can reasonably be inferred, then one useful strategy is to estimate the upper mantle contribution via measurements of SKS splitting intensity as a function of backazimuth (Fig. 2a; Chevrot 2000; Creasy *et al.* 2021). Examples of such measurements for synthetic seismograms for simple models with a single layer of anisotropy beneath the receiver are shown in Fig. 3. Specifically, we run simulations for models with HTI, olivine A-type and olivine C-type elastic tensors, as shown in Figs 3a–c. As eq. (1) shows, *SI* is expected to behave like a ($\delta t \sin 2\theta$)-curve as a function of backazimuth. By fitting such a function to the measurements, the best-fitting receiver side splitting parameters can be determined. While the $\sin 2\theta$-fit matches the measurements for HTI virtually perfectly (Fig. 3a), in the case of more realistic upper mantle elastic tensors, slight deviations from the simplest predictions are introduced (Figs 3b and c).

Once the splitting due to receiver side anisotropy has been accurately determined, we can conduct an explicit correction for this contribution (Fig. 2b). For example, teleseismic *S* phases recorded

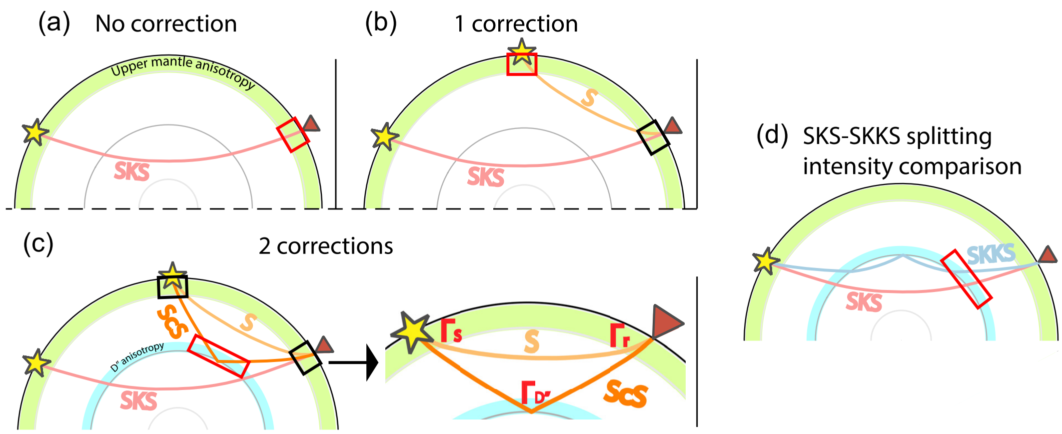

Figure 2. Schematic representation of the shear wave splitting techniques investigated in this paper, including the raypaths of the phases involved in these techniques. Red boxes represent the anisotropy we attempt to resolve and black boxes the anisotropy that we correct for. Yellow stars show sources and red triangles receivers. Raypaths of SKS (light red), SKKS (blue), S (yellow) and ScS (orange) are represented by solid lines. (a) Receiver side associated splitting is usually determined by measuring SKS splitting over a range of backazimuths. (b) If the receiver side anisotropy has been determined using SKS, *S* phases can be corrected for this contribution to estimate the contribution from source side anisotropy. (c) For S-ScS differential splitting, SKS phases (over the full backazimuthal range) are used to resolve receiver side anisotropy, represented by the splitting operator Γ_r (left-hand panel). Then S and ScS phases are corrected for this contribution. Source side splitting (Γ_s, left-hand panel) is then determined from the corrected S phase, which can then be applied to the ScS from the receiver-side-corrected seismogram to resolve D'' anisotropy ($\Gamma_{D''}$, left-hand panel) by applying corrections for the various splitting operators in the correct order (Wookey *et al.* 2005). (d) SKS-SKKS differential splitting intensity measurements are used to resolve lowermost mantle anisotropy. The method is based on the observation that SKS-SKKS raypaths are very similar in the upper mantle but diverge in the lowermost mantle (both in terms of the mantle volume sampled and in terms of the propagation direction).

at a station beneath which the anisotropy is known can be corrected to measure the source side anisotropy influencing the waveforms. In the context of our synthetic simulations, we can determine splitting due to source side anisotropy in two ways. First, we can run simulations that include source side anisotropy, but no receiver side anisotropy, and directly measure the source-side associated splitting parameters from the synthetics. Secondly, we can run simulations that incorporate both source and receiver side anisotropy in the simulation. Then we determine the receiver side anisotropy using SKS phases as described above and use this information to correct for the receiver side anisotropy contribution, thus we isolating the source side anisotropy contribution. Subsequently, we measure the splitting parameters associated with the source side. These measurements can then be compared with the direct measurements of source side splitting in the absence of receiver side anisotropy.

Similarly, for the S-ScS differential splitting technique (Fig. 2c; Wookey *et al.* 2005), explicit anisotropy corrections have to be conducted. Again, the receiver side anisotropy is determined using SKS phases, expressed as the splitting operator Γ_r (δt, ϕ) in Fig. 2c. After correcting for this contribution, the method assumes that the corrected *S* and ScS phases from the same earthquake are both affected similarly by seismic anisotropy on the source side (Γ_s), while only the ScS potentially experiences D'' anisotropy ($\Gamma_{D''}$). This argument is based on their similar raypaths in the upper mantle beneath the source. Thus, Γ_s can be determined from the corrected *S* phase, and the ScS phase can subsequently be corrected for this contribution to isolate the splitting parameters associated with D'' anisotropy ($\Gamma_{D''}$). Again, we can choose to incorporate different combinations of anisotropic layers into our simulations through several different approaches. First, we can directly measure the lowermost mantle associated splitting parameters in absence of upper mantle anisotropy. Secondly, we run simulations that only incorporate seismic anisotropy in the upper mantle on the source side, in absence of receiver side anisotropy. Then we apply the S-ScS differential splitting technique, effectively testing whether the source-side corrections are accurate for the S-ScS splitting method. Thirdly, we incorporate anisotropy in the upper mantle on source and receiver side as well as in the lowermost mantle and apply the S-ScS differential splitting technique doing the full set of corrections. The lowermost mantle associated splitting parameters determined in absence of upper mantle anisotropy can then be compared to those determined after doing the explicit corrections to assess the method's accuracy.

Another strategy to identify lowermost mantle anisotropy relies on measuring splitting for pairs of phases that have similar raypaths in the upper mantle but dissimilar raypaths at the base of the mantle. Specifically, differential splitting measurements from SKS and SKKS phases for the same source–receiver pair (Fig. 2d) are often used. Discrepant splitting can either be defined in terms of splitting differences in splitting parameters (ϕ, δt; e.g., Niu & Perez 2004; Long 2009; Lynner & Long 2014; Asplet *et al.* 2020) or in terms of differences in splitting intensity (e.g., Deng *et al.* 2017; Reiss *et al.* 2019; Lutz *et al.* 2020) The polarization direction of SK(K)S waves is purely SV due to the *P* to *S* conversion at the CMB in absence of seismic anisotropy; thus, only seismic anisotropy on the receiver side leg of the raypath has to be considered. The raypaths of SKS and SKKS phases at the relevant distances are almost identical in the upper mantle but diverge substantially in the lowermost mantle (Fig. 2d); the phases sample different regions of the D'' layer and also propagate through the lowermost mantle at different directions. This is why substantial differences in splitting can mainly be attributed to contribution from the lowermost mantle. SKS-SKKS splitting intensity comparisons have previously been shown to reliably reflect contributions from the lowermost mantle, as long as only relatively large differences in splitting intensity are interpreted (Tesoniero *et al.* 2020). This previous study, however, did not include simulations with both lowermost mantle and upper

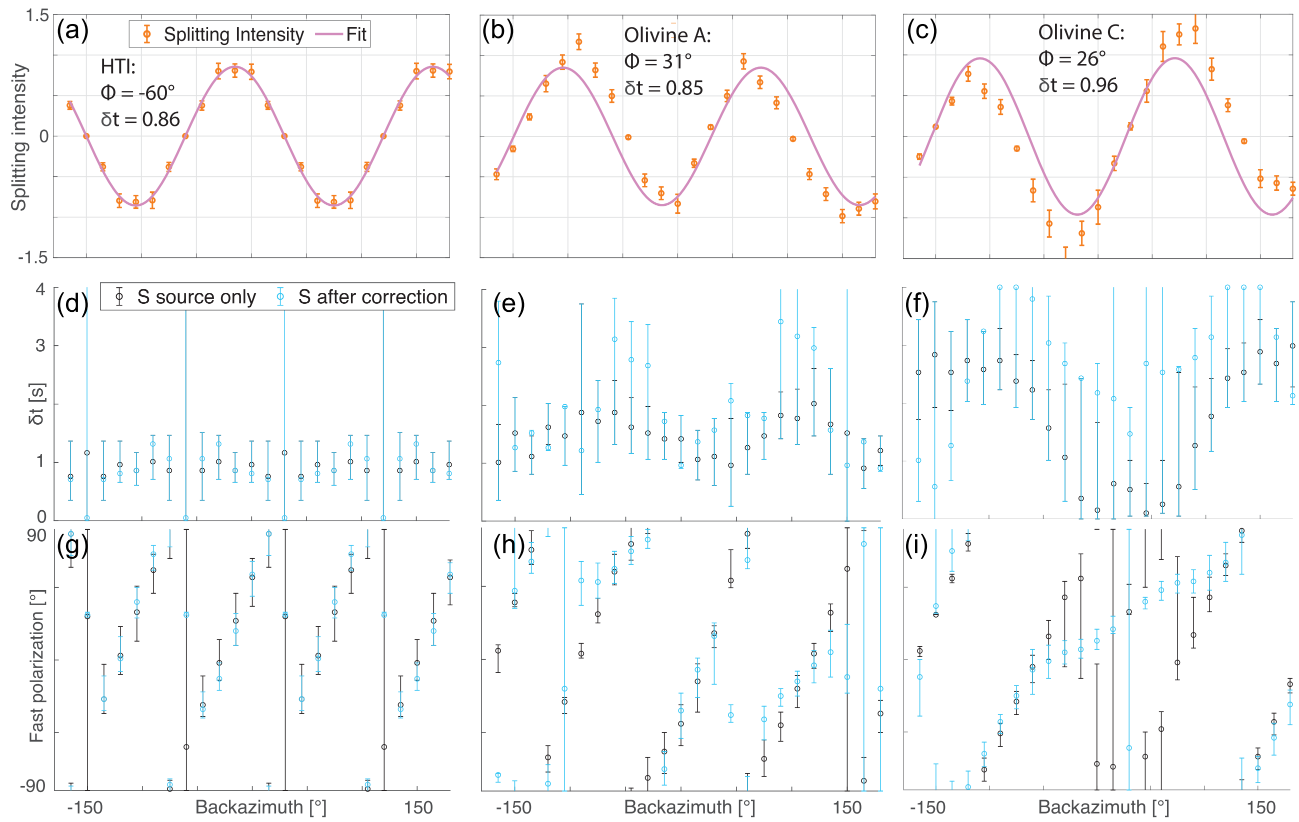

Figure 3. Results from simulations designed to test the accuracy of receiver side anisotropy corrections. (a–c) Analysis of receiver-side splitting parameters measuring *SI* as a function of backazimuth for SKS phases for various upper mantle anisotropy scenarios (HTI – a; olivine A-type – b; olivine C-type – c). Orange circles indicate splitting intensity measurements with the error bars showing 95 per cent confidence regions determined using SplitRacer (Reiss & Rümpker, 2017). Fast directions and delay times, obtained by fitting a sin(2θ)-curve to the splitting intensity data as a function of backazimuth, are noted on the corresponding subplots. (d–i): Delay times (d–f) and fast polarization directions (g–i) associated with source side anisotropy determined using direct teleseismic *S* phases, as schematically shown in Fig. 2b. Black circles show measurement values for simulations for which only source side anisotropy is incorporated into the input models (and therefore represent the 'expected' signal after receiver-side corrections). Blue circles show values after receiver side correction for simulations that use input models with source side and receiver side anisotropy (legend). 95 per cent confidence intervals are again shown by error bars. The receiver side splitting parameters used for the correction are those shown in panels for the corresponding anisotropy scenario (a–c). Panels (a, d, g) are for a HTI elastic tensor, (b, e, h) for an olivine A-type elastic tensor and (c, f, i) for an olivine C-type elastic tensor in the upper mantle.

mantle anisotropy, and therefore did not investigate a broad range of possible upper mantle contributions to SK(K)S splitting in the context of SKS-SKKS splitting discrepancies. Here we expand on the previous results of Tesoniero *et al.* (2020) to evaluate the accuracy of the method in light of the (ray theoretical) assumptions built into it.

3 EVALUATING ASSUMPTIONS OF COMMONLY USED SPLITTING TECHNIQUES: EFFECTS OF UPPER MANTLE ANISOTROPY

3.1 Accuracy of receiver side corrections and applications to source-side S splitting

Explicit corrections for the effect of upper mantle anisotropy on the receiver side are commonly applied, and these corrections are typically done in a ray theoretical context and with simplified assumptions about the geometry and symmetry of the anisotropic medium. Such corrections also typically assume that the incidence angles of the phases used to estimate the upper mantle splitting contribution (typically SKS) are similar enough that the studied phases (e.g., *S* or ScS) undergo identical splitting. In order to test the validity of these assumptions, we run a series of wavefield simulations that incorporate both source- and receiver-side anisotropy in the upper mantle, correct the synthetic phases for splitting using conventional approaches, and compare the measured splitting after correction to that predicted for synthetic waveforms obtained from simulations with no receiver-side contribution. We first focus on understanding receiver side corrections in the context of source-side direct *S* measurements (e.g., Russo & Silver 1994; Russo *et al.* 2010; Eakin & Long 2013; Eakin *et al.* 2018). To do this, we simulate earthquakes 120° away from the station arranged in a circular geometry around the receiver (see Fig. 1) and determine the splitting intensity as a function of backazimuth for SKS phases in the synthetic seismograms (Figs 3a–c). Then, we calculate the best-fitting receiver-side associated splitting parameters based on these splitting vectors. We next simulate sources at an epicentral distance of 60° from the receiver in an otherwise similar geometry (Fig. 1). The *S* phases from these simulations experience source and receiver side anisotropy; the *S* phases are corrected for receiver side splitting, and we measure the remaining splitting on the corrected seismogram (Fig. 2b). In this way, the source-side associated splitting parameters can be derived (blue signs in

Figs 3d–i). We can then compare these source-side anisotropy-associated splitting parameters (derived after explicit upper mantle corrections) with splitting parameters measured from synthetic *S* phases generated for an input model that only includes anisotropy on the source side, with no receiver side anisotropy (black signs in Figs 3d–i).

We carry out this modelling exercise using three different upper mantle anisotropy models (on both the source and the receiver side): an HTI upper mantle (Figs 3a, d and g), an olivine A-type upper mantle (Figs 3b, e and h) and an olivine C-type upper mantle (Figs 3c, f and i). Results for E-type olivine are shown in the Supporting Information. The A-, C- and E-type olivine tensors are aligned assuming horizontal simple shear in the upper mantle. Fig. 3 illustrates some limitations of this approach to upper mantle corrections for different anisotropic tensors. The precision of the correction appears to at least partly depend on how well the ($\delta t \sin 2\theta$)-fit matches the receiver side splitting intensity, which in turn depends on the symmetry of the elastic tensor. Specifically, the splitting intensity is an almost perfect ($\delta t \sin 2\theta$)-curve as a function of backazimuth for HTI (Fig. 3a); hence, the use of a correction derived from this fit for the receiver side anisotropy is relatively accurate (Figs 3d and g). The situation is different, however, for the more complicated olivine elastic tensors, because there are subtle deviations from the $\sin 2\theta$-fit due to the lower symmetry of the tensors. Comparing the splitting parameters obtained for the corrected *S* phases versus those obtained for the models that do not include receiver side anisotropy, we see that there are significant deviations at some backazimuths. In general, the correction works fairly well for the fast polarization direction ϕ (Figs 3h–i), given that measurements with large error bars (which are often associated with the imperfect corrections) ($\sim\pm 20^\circ$ for ϕ) would not be interpreted for real data in any case. The time lag δt after the correction shows more significant deviations from the expected value for A- and C-type fabric (Figs 3e–f), suggesting that there may be considerable uncertainty in the values of source-side splitting delay time estimates in real data. The results for olivine E-type in the upper mantle are shown in Fig. S1 and are consistent with the observations from Fig. 3, although the error bars on the fast polarization direction ϕ tend to be larger than for the A- and C-type olivine examples from Fig. 3.

In general, our modelling experiments show that the assumptions built in to upper mantle corrections for source-side *S* splitting are generally accurate enough to yield reliable information on source-side anisotropy, but there are some caveats. Although the incidence angles of SKS and direct teleseismic *S* are different, the approximation of similar splitting of these phases that is built in to the method works well for upper mantle anisotropy with HTI symmetry. For more complicated (and perhaps more realistic) elastic tensors, however, inaccuracies in the corrections are introduced, and some caution must be applied to the interpretation of source-side *S* splitting measurements in light of this finding. We expect that our results for upper mantle corrections for direct *S* splitting studies should also be more generally applicable to other types of splitting studies that incorporate explicit upper mantle corrections, for example, studies of lowermost mantle anisotropy that correct SK(K)S phases for the effect of upper mantle splitting and measure residual splitting (e.g., Lynner & Long 2012; Long & Lynner 2015; Ford *et al.* 2015). As for direct *S* splitting, for such studies the different angle of incidence for *S* and SK(K)S phases can be expected to lead to minor inaccuracies, as well as some inaccuracies in the determination of upper mantle splitting.

3.2 Accuracy of source-side upper mantle corrections and application to S-ScS differential splitting

For ScS-differential splitting, two explicit anisotropy corrections are applied (Fig. 2c). First, a receiver side correction is applied, very similar to the type of correction explored in Section 3.1. Next, a source side correction is applied. To do this, the source-side contribution to splitting of both S and ScS phases from the same source–receiver pair is estimated using direct *S* as the 'reference' phase. The ScS waveforms are then corrected for the effect of upper mantle anisotropy on the source side (as experienced by the direct *S* phase), while also taking into account the possibility of splitting due to lowermost mantle anisotropy. This source-side upper mantle anisotropy correction is similar in spirit to the receiver-side correction investigated in Section 3.1, but with the potential added complication of the CMB reflection of the ScS phase, which is not typically explicitly taken into account in differential S-ScS splitting studies. Here we extend our investigation to consider multiple upper mantle corrections in the context of differential S-ScS splitting. In this section, we examine the accuracy of the source-side upper mantle anisotropy corrections in isolation, without considering a contribution from the receiver side. In Section 4, we carry out modelling experiments that explicitly include multiple layers of anisotropy (potentially including upper mantle source side, lowermost mantle, and upper mantle receiver side) to evaluate the method as a whole and propose new strategies for improving the accuracy of differential S-ScS splitting measurements.

As a start, we simulate an earthquake in an epicentral distance of 60° from the station. We choose the initial source polarization so that S and ScS phase are initially fully SV polarized. In our input model we only incorporate HTI source side anisotropy and no receiver side or lowermost mantle anisotropy. We then measure the splitting of both the synthetic S and ScS phases, as shown in Fig. 4—this splitting should only be due to splitting in the upper mantle near the source, as the rest of the model is isotropic. This figure shows both the radial (*R*) and transverse (*T*) components of *S* and ScS phases (left-hand panel) as well as the measured splitting parameters (ϕ-δt-planes, right-hand panel). In the left-hand panel, yellow lines represent the predicted arrival times of *S* and ScS for the PREM model, which was used as the background model for the non-anisotropic portions. Fig. 4 shows that the measured splitting parameters for the *S* and the ScS phases differ substantially, even though both phases travelled through the same source side anisotropy. The reason for this is visible in the waveforms: while the transverse components of the *S* and the ScS arrival have nearly identical shapes, the radial component of the ScS is a sign-flipped version of the radial component of the *S* phase. This sign flip on the radial component means that the apparent splitting parameters are different, even though the phases have sampled the same anisotropy near the source. This observation implies the straightforward correction for source-side anisotropy for *S* and ScS phases that is typically applied to study lowermost mantle anisotropy, which does not explicitly account for the effect of the CMB reflection for ScS (e.g., Wookey *et al.* 2005; Nowacki *et al.* 2010; Wolf *et al.* 2019), can be inaccurate.

To elaborate on this point further, it is clear from Fig. 4 that the reflection at the CMB (and the associated change to the radial component waveform) affects the estimate of splitting parameters. Specifically, upon reflection, the transverse component (SH wave) will fully reflect at the CMB without a phase shift, because *S* waves cannot propagate through the liquid outer core. On the other hand,

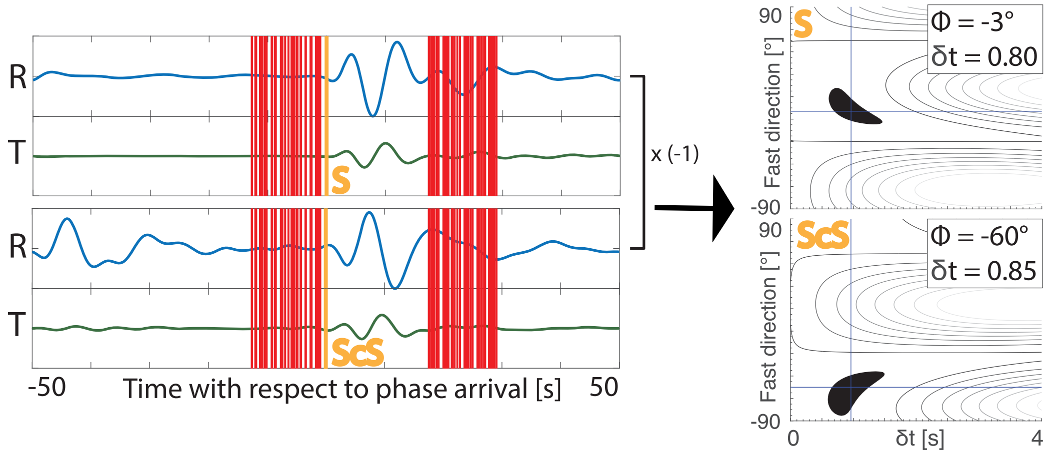

Figure 4. Illustration of the influence of source side anisotropy on *S* and ScS phases, in absence of receiver side and lowermost mantle anisotropy. Radial-Transverse (*R-T*) seismograms for the *S* (left-hand panel; top) and the ScS phase (left-hand panel; bottom) for the same simulation. Phase arrivals are indicated by yellow lines. 50 randomly selected measurement windows are indicated by red lines. The measured splitting parameters are shown to the right in the ϕ-δt-plane with the black regions indicating 95 per cent confidence regions (with contour lines showing different transverse energy component levels). The measured source-side splitting parameters are different for *S* and ScS, due to the approximate sign-flip of the radial component of ScS compared to the radial of the *S*, while transverse components are virtually identical.

the SV energy on the radial component will couple with the *P* wave in the outer core, with some SV energy getting transmitted to *P*, and thus its phase (and amplitude) will be affected. As originally formulated by Wookey *et al.* (2005) and as implemented in a number of observational studies (e.g., Wookey & Kendall 2008; Nowacki *et al.* 2010; Ford *et al.* 2015; Creasy *et al.* 2017; Wolf *et al.* 2019), the S-ScS differential splitting technique relies on the assumption of an approximately horizontal raypath of ScS and therefore does not explicitly take into account the CMB reflection. While some studies (Nowacki & Wookey 2016; Wolf *et al.* 2022) have shown that the horizontal raypath approximation for ScS splitting may be an oversimplification in many cases, the precise effect of the reflection is not generally considered in the context of lowermost mantle splitting studies.

In order to examine the influence of the ScS CMB reflection more precisely, we assume PREM-like P and S velocities on both sides of the CMB and analyse the reflection coefficients for a range of reasonable source depths and epicentral distances. The real and imaginary parts of the SV reflection coefficient as a function of distance are shown for SV portion of the ScS in Fig. 5a, for both a 0 km deep source and a 500 km deep source. For S-ScS differential splitting, the epicentral distance range between 60° and 80° is most relevant, as this range is typically used in splitting studies. Between 60° and 80° epicentral distance, the real part of the reflection coefficient is approximately −1, with its minimum absolute value of 0.8 at 60° distance for a 0 km deep source. A real part of −1 for the reflection coefficient would correspond to a perfect sign flip, if the imaginary part is zero. However, the imaginary part is non-zero, indicating a deviation from a perfect sign flip in this distance interval. The precise value of the phase shift is shown in Fig. 5b as a function of epicentral distance. While the phase shift is almost precisely 180° for 60° distance and a 0 km deep source, it will generally deviate from a perfect sign-flip in the distance interval 60° to 80°. The maximum deviation from a sign-flip is reached at approximately 70° distance (for both source depths), shifting the phase by ∼160°.

Strictly speaking, the precise phase shift and the precise loss of amplitude of the ScS due to the CMB reflection have to be

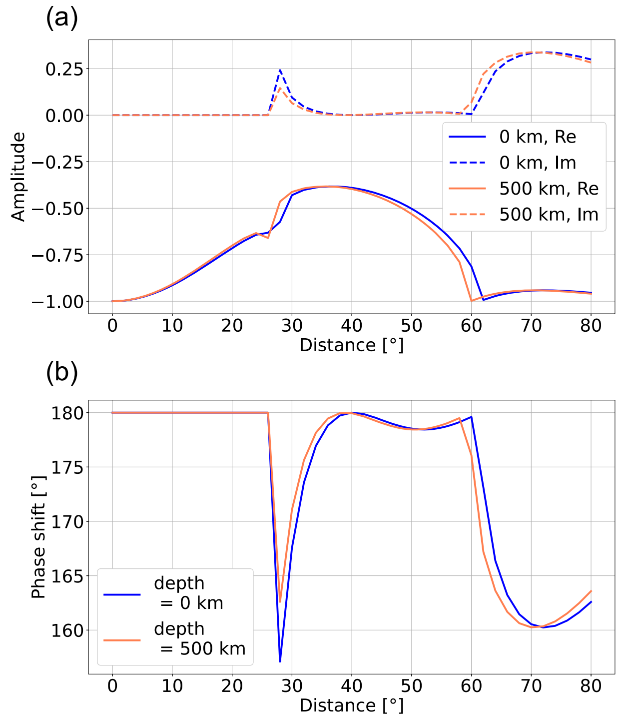

Figure 5. Influence of the CMB reflection on SV portion of the ScS phase for seismic velocities above and below the CMB predicted for the PREM (Dziewonski & Anderson 1981) velocity model solving the corresponding equations from Chapman (2004), chapter 6. Predictions for a focal depth of 0 km are shown in blue and for 500 km focal depth kilometres in yellow. (a) Real (solid lines) and imaginary parts (dashed lines) of the reflection coefficient are shown as a function of epicentral distance. For distances larger than 60° the real part of the reflection coefficient has an absolute value of approximately 1, indicating that the amplitude will not change much through the reflection. (b) Phase shift of the radial component of the ScS as a function of epicentral distance. For epicentral distances larger than 60°, the phase shift is between 160° and 180° (=perfect sign flip).

considered for the source side correction of S-ScS differential splitting. The radial component would have to be rotated differently depending on the phase shift and multiplied by a certain factor to account for the amplitude difference. However, because in the 60° to 80° distance interval the real part of the reflection coefficient is consistently approximately −1 and the phase shift deviates at most by ∼20° from 180°, in Section 4 we will show that approximating the influence of the reflection as a simple sign flip of the radial component is precise enough to carry out accurate source side corrections for the S-ScS differential splitting technique. This way, when the initial polarization of the *S* wave is known (or estimated from the long axis of the particle motion ellipse), the source side associated splitting parameters for ScS can be predicted by measuring *S* splitting, and an accurate correction can be applied that takes into account the phase shift at the CMB.

3.3 Multiple layers of anisotropy and the commutativity of the splitting intensity

Measurements of SK(K)S splitting intensity, and in particular measurements of differential SKS-SKKS splitting intensity, have been used to infer contributions to the splitting of core phases from anisotropy in the lowermost mantle (e.g., Deng *et al.* 2017; Grund & Ritter 2018; Asplet *et al.* 2020; Reiss *et al.* 2019; Wolf *et al.* 2019; Lutz *et al.* 2020). A key assumption built into the differential splitting intensity approach for SKS-SKKS waves is the idea that the splitting intensity is commutative (e.g., Chevrot 2000, 2006; Silver & Long 2011), and therefore the splitting intensity contribution from different layers can be summed to obtain the total splitting intensity value.

3.3.1 Testing the commutativity of the splitting intensity

Here we test the assumption that the splitting intensity is commutative for different anisotropy strengths, initially in the context of simulations that incorporate multiple layers of anisotropy in the upper mantle that are sampled by direct teleseismic *S* waves on both the source and the receiver side. We carry out simulations that include olivine A-type fabric in the upper mantle, first only at the source side (as a reference case) and then also at the receiver side (as a case with multiple layers of anisotropy). We set the anisotropic geometry such that the *S* phase samples identical anisotropy (and thus undergoes identical splitting, at least from a ray theoretical point of view) on both source and receiver side. The epicentral distance for these simulations is again 60° and the focal mechanism is as shown in Fig. 1. We repeat this exercise for different layer thicknesses, which correspond to different integrated strengths of anisotropy experienced by the wave along the raypath. This allows us to test the (ray theoretical) expectation that the splitting intensity should be twice as large for models with both source and receiver side anisotropy than for models with anisotropy only on the receiver side. These results of these simulations are shown in Fig. 6. If the assumption that the splitting intensity is commutative holds, then the two-layer case (black symbols) should agree with the predictions made by doubling the splitting intensity for the one-layer case (blue symbols), as in Fig. 6a. We find, however, that with increasing layer thickness (or, equivalently, increasing integrated strength of anisotropy sampled by the wave), the assumption of commutativity becomes less accurate (Figs 6b and c). The assumption of commutative splitting intensity does hold, however, for total splitting intensity values in between −1 and 1 (black dashed lines in Fig. 6), regardless of the layer thicknesses themselves. This observation is not completely surprising, given that the assumption in the splitting intensity definition (eq. 1) that the delay time is much smaller than the period of the wave breaks down for strong anisotropy. However, this factor is typically not explicitly taken into account in differential SKS-SKKS splitting intensity studies. Interestingly, δt for the simulations shown in Fig. 6 approximately doubles for a doubled anisotropic layer thickness (in contrast to SI), while ϕ is largely independent of layer thickness, as would be expected (Fig. S2). The extent to which *SI* is commutative likely depends on the dominant period of the signal, which for our synthetic simulations is ∼8 s. For real data, the dominant period of the signal may be somewhat variable and may tend to be slightly larger. We will apply our insights into the commutativity of *SI* measurements to suggest improvements in methods for differential SKS-SKKS splitting intensity studies in Section 4.2.

3.3.2 Implications of limited SI commutativity for SKS-SKKS differential splitting

Although we do not explicitly incorporate lowermost mantle anisotropy in our models here, the limited commutativity of the splitting intensity for strong splitting is directly applicable to SKS-SKKS differential splitting, which can be regarded as a special case of two-layered anisotropy: If the splitting intensity is commutative (weak splitting) and the anisotropy sampled at the base of the mantle is different for SKS and SKKS phases, then the SKS-SKKS differential splitting technique will work well (Tesoniero *et al.* 2020). In case of strong splitting (in lower or upper mantle), splitting intensity values of SK(K)S will not necessarily accurately reflect the strength of (integrated) anisotropy sampled along the raypath anymore. In this case, the SKS-SKKS differential splitting intensity method can fail. Fortunately, this limitation can be overcome relatively easy by taking two precautions. First, SKS-SKKS pairs should not be interpreted in cases for which the 95 per cent confidence interval of one of the phases includes an absolute *SI*-value larger than 1. We choose this value based on the results displayed in Figs 7 and S3. Secondly, only large differences in *SI* (>0.4) should be regarded as unequivocal evidence for lowermost mantle anisotropy. Our results indicate that if both these precautions are taken, the SKS-SKKS differential splitting intensity method will lead to an improved reliability, as discussed further in Section 4.1.1.

4 NEW STRATEGIES FOR MEASURING LOWERMOST MANTLE ANISOTROPY

4.1 The S-ScS differential splitting method: strategies for improvement

Here we investigate the accuracy of an improved algorithm for differential S-ScS splitting that explicitly takes into account the phase shift at the CMB when carrying out the correction for source-side splitting. We first investigate whether a strategy that approximates the effect of the reflection on the SV portion of the ScS phase as a simple sign-flip that preserves the amplitude is sufficiently accurate for differential S-ScS splitting studies. Secondly, we present a series of simulations that investigates the limitations and uncertainties of the differential S-ScS method when there is upper mantle anisotropy both near the source and near the receiver (that is, accounting for three separate layers of anisotropy that are sampled progressively by the downgoing and upgoing legs of the ScS phase). It is important

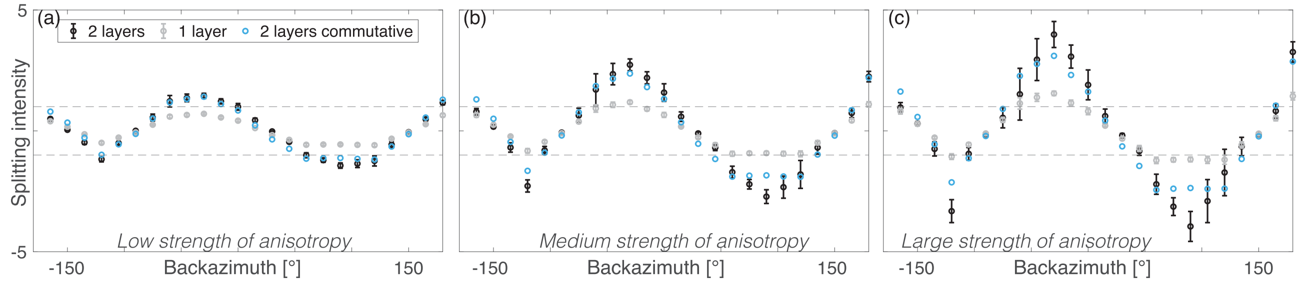

Figure 6. Measured splitting intensity values for synthetic waveforms derived from simulations with different strengths of splitting due to upper mantle anisotropy (assuming A-type olivine) for a source–receiver distance of 60°. The splitting intensity is measured as a function of backazimuth from *S* phases for simulations that only include source side anisotropy (grey) and source+receiver side anisotropy (black), with the error bars indicating 95 per cent confidence intervals. The backazimuth corresponds to the direction from which the elastic tensor is sampled. By design, the seismic anisotropy that the seismic wave samples on source and receiver side is identical. Thus, if the splitting intensity is additive, the splitting intensities measured in presence of source+receiver side anisotropy will match twice the splitting intensity associated with the source side only (light blue). Black dashed lines indicate splitting intensity values of 1 and −1. (a) Simulation for a small layer thickness (specify value), which leads to relatively weak splitting due to upper mantle anisotropy. For this case, the splitting intensity is approximately additive. (b) Simulation for a medium layer thickness (specify value; medium strength of splitting due to anisotropy in the upper mantle): For large absolute splitting intensity values the splitting intensity is not strictly commutative. (c) For a thick layer (specify value; strong splitting due to upper mantle anisotropy), the assumptions built into the splitting intensity formula break down, and *SI* becomes non-commutative.

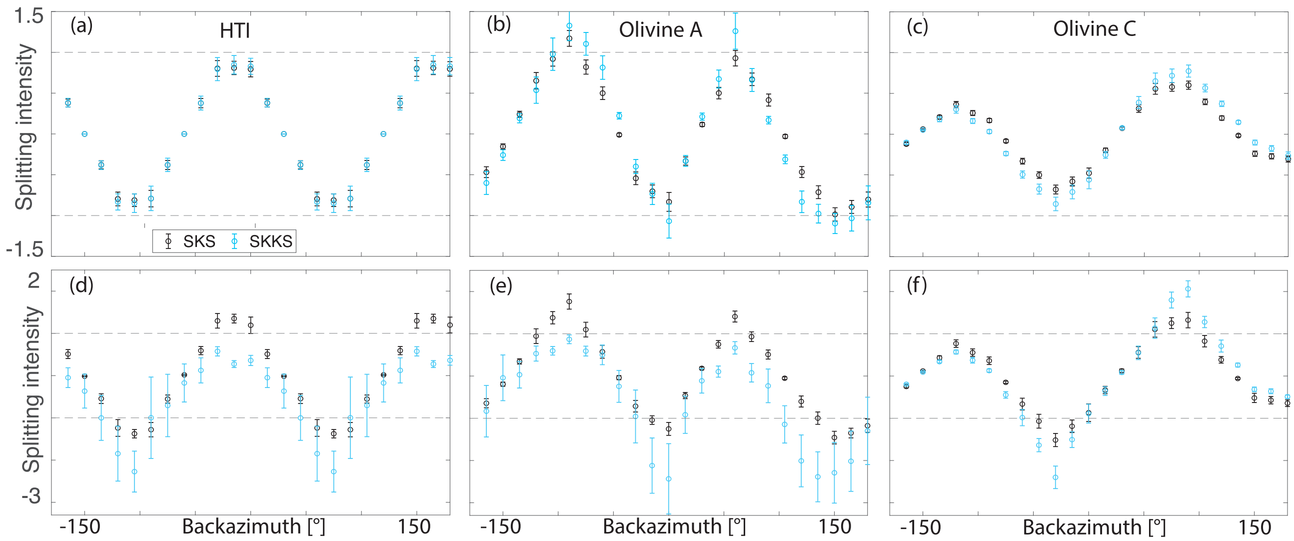

Figure 7. Splitting intensity measurements for SK(K)S phases in the presence of only upper mantle anisotropy for an epicentral distance of 120°. The results are shown as a function of backazimuth, which corresponds to the direction from which the elastic tensor is sampled. Black dashed lines indicate splitting intensity values of 1 and −1. Black circles indicate SKS and blue circles SKKS splitting intensities, with error bars showing 95 per cent confidence intervals. Measurements were taken for HTI (a, d), olivine A-type (b, e) and olivine C-type (c, f) anisotropy in the upper mantle. The thickness of the anisotropic layer in the upper mantle is moderate (HTI: 180 km; olivine A: 170 km; olivine C: 120 km) for the simulations in panels (a–c) and large (HTI: 300 km; olivine A: 230 km; olivine C: 250 km) for the simulations in panels (d–f). For the thick anisotropic layer, upper mantle anisotropy may lead to strong SKS-SKKS splitting intensity discrepancies for many backazimuths, which may erroneously be interpreted as being due to lowermost mantle anisotropy. We suggest a threshold value above which discrepant SKS-SKKS splitting intensities can be observed even in the absence of lowermost mantle contribution of 1 (that is, *SI*-values of either phase are greater than 1).

to remember that for actual data, the effects of the phase shift due to the CMB reflection on the source-side correction will vary, depending on several factors. First, the initial polarization of the S/ScS waves is important: depending on the relative amounts of SV vs. SH polarized energy (which in turn depends on the earthquake focal mechanism), the effect of the CMB reflection on the source-side correction will range from significant to non-existent. Secondly, for the case where anisotropy near the source is weak or non-existent, or for the case in which the initial polarization of the S/ScS phases is aligned with a slow or fast direction of the medium and the phases undergo no splitting, no source-side correction is needed and the effect of the CMB reflection on the correction is therefore unimportant. (However, the effect of the CMB reflection on splitting due to lowermost mantle anisotropy on the downgoing leg of the ScS phase can still be important.) We therefore initially focus on the effects of the reflection using a 'worst case' scenario, with an initial polarization that is purely SV. We also investigate cases for which there is a large deviation from the purely 180° phase shift, in order to show that approximating this phase shift with a simple sign flip is valid.

4.1.1 *Accounting for effects of the CMB reflection on source-side corrections*

First, we simulate earthquakes at a depth of 0 km in a distance of 60° to the receiver. At that distance, the radial component of ScS almost perfectly flips its sign due to the CMB reflection; however, the real part of the reflection coefficient for SV is −0.8, which is the minimum absolute value in the distance interval between 60° and 80°, indicating the maximum loss of amplitude due to the reflection. We assess the effect of the source-side correction on lowermost mantle splitting estimates by running simulations with progressively more complex anisotropy scenarios (Fig. 8). First, we only incorporate lowermost mantle anisotropy in our input model; in this case, no upper mantle corrections are needed and the measured splitting parameters ϕ and δt directly reflect the effect of lowermost mantle anisotropy. Results from these simulations are shown as black crosses in Fig. 8, with 95 per cent confidence intervals. In these simulations, we rotate the Ppv elastic tensor describing anisotropy in the lowermost mantle such that the tensor is sampled from precisely the same direction over all backazimuths (following the strategy laid out by Wolf *et al.* 2022). By keeping the direction from which the D'' elastic tensor is sampled the same, we ensure that any differences in the results of our simulations can clearly be attributed to the effects of the different corrections, rather than the effects of sampling the tensor from different orientations. For the second class of simulations, we keep the lowermost mantle anisotropy the same as in the previous set of experiments and add seismic anisotropy in the upper mantle at the source side; for these simulations, source-side corrections are necessary. We apply the corrected S-ScS differential splitting technique to the synthetic waveforms, assuming that the CMB reflection results in a perfect sign flip of the radial component of ScS, while preserving the (absolute value of) amplitude. Estimates of splitting parameters due to lowermost mantle anisotropy obtained from these simulations are shown in light blue in Fig. 8. In the third set of simulations, we also add receiver side anisotropy. The splitting associated with the receiver side is estimated using SKS phases as in Section 3.1; we then correct the synthetic waveforms for the effect of splitting beneath the receiver. We then estimate the lowermost mantle splitting parameters (shown in yellow colour in Fig. 8) as we did for the second set of simulations.

We carried out this exercise using three different elastic tensors in the upper mantle (incorporating the same elastic tensor at the source and receiver side). For HTI (Figs 8a and b), the splitting parameters obtained in absence of upper mantle anisotropy agree very well with those obtained after correcting for upper mantle splitting. For olivine A-type (Figs 8c and d) and C-type (Figs 8e and f), only the measurements for the fast polarization direction ϕ are reliable if corrections are applied; we find that the delay times are generally not accurately retrieved. This is similar to our finding in Section 3.1 applied to source-side splitting estimates for direct *S* waves, and suggest that estimates of δt for lowermost mantle splitting should not be overinterpreted in cases where significant upper mantle corrections are applied (particularly if there is reason to believe that the upper mantle anisotropy deviates from HTI symmetry). As expected, we find that when receiver side anisotropy is absent, the estimates of lowermost mantle splitting are more precise than for cases that include receiver side anisotropy in the input models.

In general, the simulation results shown in Fig. 8 demonstrate that the phase shift at the CMB can accurately be accounted for in our 'worst case' scenario of a purely SV initial polarization. We next repeat our simulations for initially SH-polarized *S* and ScS waves, as well as an SV-polarized scenario with a Br elastic tensor in the lowermost mantle. These results are shown in Figs S4 and S5. Additionally, we ran the same simulations for olivine E-type in the upper mantle (Fig. S6) as well as for a focal depth of 500 km (Fig. S7). Overall, these results are very similar to those in Fig. 8, demonstrating that our approach to the source-side corrections need not depend on the initial polarization of the wave or on the character of lowermost mantle anisotropy or the focal depth of the earthquake.

Next, we return to simulations with a Ppv elastic tensor and purely SV polarized S-ScS phases and revisit the the question of whether the CMB reflection can be approximated as a sign flip on the radial component. This time, we choose a distance of 67° and an earthquake depth of 0 km (the depth is intentionally kept at 0 km to keep this test as comparable to the previous test as possible). For this distance, one would expect a relatively large deviation from a 180° phase-shift (Fig. 5). We note that the the phase shift can be expected to be slightly larger than for 67° at distances up to 73°; however, contamination from other phases cannot be excluded in this distance range (Wolf *et al.* 2022). At the selected distance, there is almost no change to the amplitude due to the reflection (Fig. 5). For this case, we again test whether a simple sign-flip approximation of the radial component is sufficient to accurately account for splitting of the downgoing ScS leg in the S-ScS differential splitting technique. The results from this test are shown in Fig. 9, which uses the same colour scheme and nomenclature as Fig. 8. We find that S-ScS differential splitting works reliably overall, although larger errors are introduced than for a distance of 60°, especially for an olivine C-type elastic tensor in the upper mantle (Fig. 9f). This implies that deviations from a perfect 180° phase shift seem to be more important than slight amplitude changes of the radial component due to the CMB reflection in affecting the accuracy of the correction. Still, we have shown that approximating the CMB reflection as a sign-flip of the radial component works well, considering that our simulation parameters have been intentionally chosen to maximize the phase shift (while avoiding contamination of other phases).

4.1.2 Investigating the limits of the S-ScS differential splitting technique

Having established the utility of accounting for the CMB reflection with a simple sign flip (that is, a 180° phase shift with no loss of amplitude), we now carry out a series of simulations designed to establish the limitations and uncertainties of the S-ScS differential splitting technique for characterizing lowermost mantle anisotropy for different elastic tensors and relative strengths of anisotropy in the upper and lowermost mantle. We now go back to a source–receiver distance of 60° and repeat similar simulations as in previous sections, this time for olivine A-type in the upper mantle. We choose to focus on A-type olivine because this is a more realistic choice than the higher-symmetry HTI tensor, and we showed in Section 3.1 that there were some deviations from predictions for receiver-side corrections with this elasticity model. Because we are now focused on exploring the limitations of the S-ScS differential splitting technique, we investigate upper mantle corrections for a lower-symmetry elasticity model for the upper mantle. Because no substantial difference in behaviour of A and C-type olivine could be observed (Fig. 3), we choose to focus on one of the tensors (A-type) here. For Fig. 10 we choose an initial SV source polarization; Fig. S8 shows the same results for an initial SH polarization of both phases. We initially choose two different relative strengths of upper and mantle anisotropy for our simulations. For the first simulation, the strength of the upper mantle anisotropy is smaller than the strength of the lowermost mantle anisotropy (Figs 10a and b), while for the second simulation upper mantle anisotropy is more dominant than the anisotropy in the lowermost mantle (Figs 10c and d). To be more precise, we do not actually change the strength of the anisotropy but instead the ratio of upper and lowermost mantle anisotropy layer

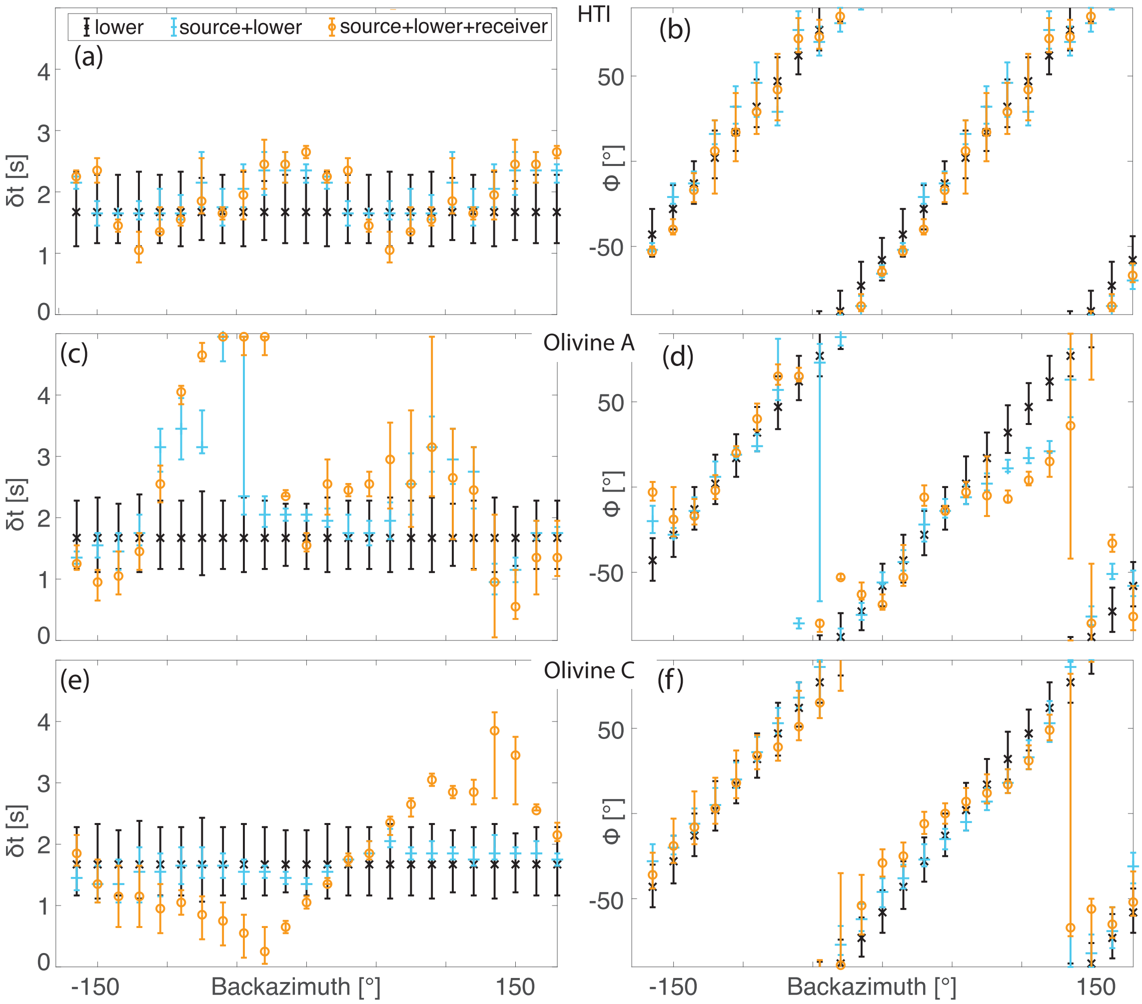

Figure 8. Estimates of lowermost mantle-associated splitting parameters δt (a, c, e) and ϕ (b, d, f) for ScS phases, after correction for upper mantle anisotropy, for models with different elastic tensors in the upper mantle: HTI (a–b), olivine A-type (c–d) and olivine C-type (e–f). All measurements are shown as a function of backazimuth, which corresponds to the direction from which the upper mantle anisotropy is sampled. We rotate the Ppv elastic tensor in the lowermost mantle in our simulations, such that it is always sampled from the same direction (and therefore the same splitting due to lowermost mantle anisotropy is expected in all simulations). The source–receiver distance for these results is 60° and the focal depth 0 km. Measurements on waveforms computed for a model with no upper mantle anisotropy (corresponding to the expected splitting signal after upper mantle corrections) are shown by black crosses. Blue plus-signs show estimated splitting parameters after correcting for the source side anisotropy implemented in the simulations in the absence of receiver side anisotropy. Yellow circles show results after applying all anisotropy corrections using the corrected S-ScS differential splitting technique for simulations that include source-, receiver side- and lowermost mantle anisotropy. In each case error bars indicate 95 per cent confidence regions. We find that, δt determined by the corrected S-ScS differential splitting technique is generally less reliable, while ϕ is more robust.

thicknesses. The layer thicknesses for Figs 10a and b were 200 km for the upper mantle anisotropy and 175 km for the lowermost mantle anisotropy; for Figs 10c and d, we choose thicknesses of 230 km (upper mantle) and 100 km (lowermost mantle). Fig. 10 shows results from both simulations with the same plotting conventions as Figs 8 and 9. In addition to results obtained using the corrected method which explicitly accounts for the phase shift at the CMB (Figs 10a and c), we also present results from the traditional ScS-S differential splitting method (Figs 10b and d), which assumes horizontal propagation through D''. We show only the fast polarization direction ϕ in the main manuscript here because we have previously shown (Figs 8 and 9) that the estimates for δt are less well resolved (for the corrected method). This is also confirmed by Fig. S9, which shows results for δt for the same simulations presented in Fig. 10.

These tests both demonstrate that the corrected method generally successfully resolves the fast polarization direction of the lowermost mantle anisotropy. However, the corrected method is less reliable for the strong upper mantle anisotropy (Fig. 10c) case, demonstrating that estimates of lowermost mantle anisotropy are more reliable in cases when the upper mantle contribution to splitting is small. In particular, we note that in this simulation, ϕ is poorly estimated between backazimuths 90° and 150°. We speculate that this may be due to imprecise receiver side corrections for this azimuth range (Fig. 3b), although this would not explain why we do not see a similar trend in the backazimuthal range −90° to −30°, for which the receiver side correction is similarly imprecise.

We also find that original S-ScS differential splitting method (assuming horizontal propagation) works acceptably well when the strength of the upper mantle anisotropy is low (Fig. 10b); however, for strong upper mantle anisotropy it becomes unreliable for the SV polarized case (Fig. 10d). This observation makes sense, because the phase shift has a particularly strong effect on the source-side

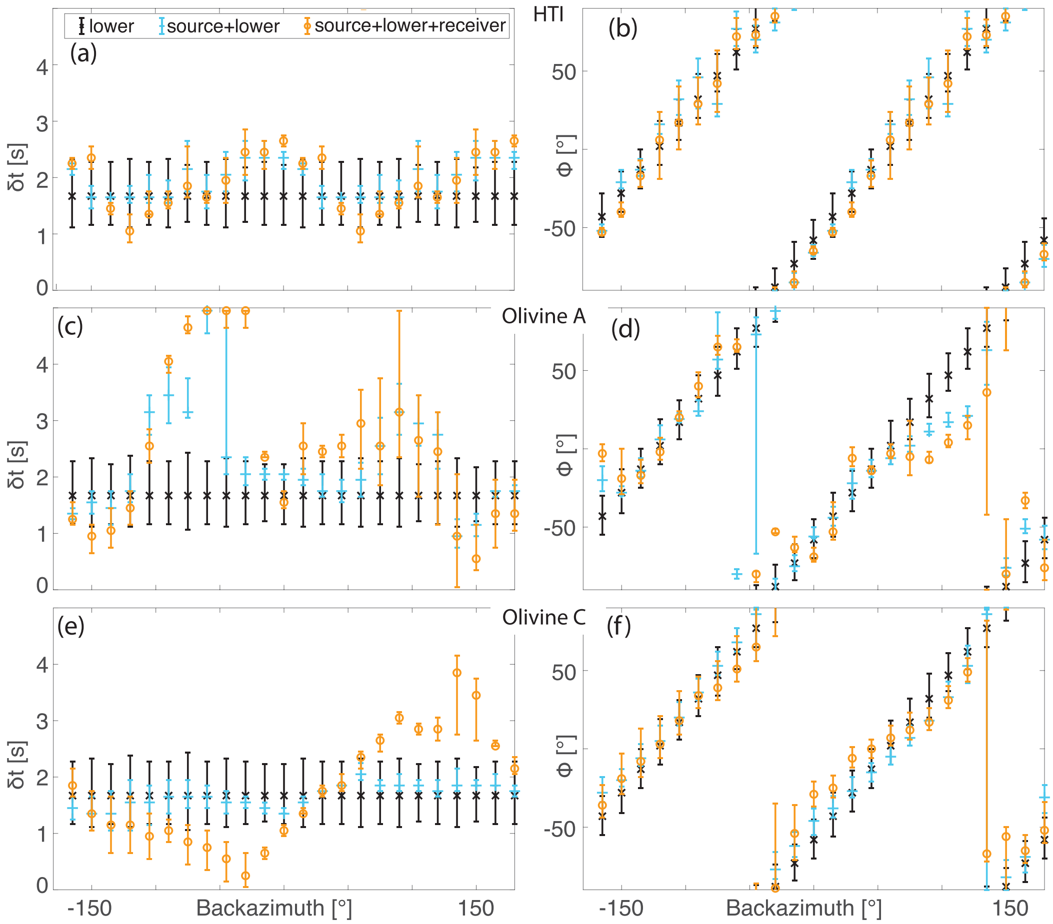

Figure 9. Same as Fig. 8, except for a source–receiver distance of 67°. Nomenclature and plotting conventions are the same as in Fig. 8.

upper mantle corrections (Section 3.2). Overall, these tests show us that the corrected S-ScS differential splitting technique is most reliable if the amount of splitting due to upper mantle anisotropy on both the source and receiver side is low, but should be treated with caution in the case of large contributions to splitting from the upper mantle. The traditional S-ScS differential splitting approach can break down if the strength of the upper mantle anisotropy is large (Fig. 10d), meaning that measurements in the literature for which a large strength of upper mantle anisotropy was corrected for, particularly for individual measurements in which the initial polarization of the wave was close to SV, should be revisited. This is the case for some measurements from our own previous work (e.g., Wolf *et al.* 2019). In general, most previously published S-ScS differential splitting papers likely include a subset of measurements for stations with strong source-side anisotropy that would benefit from being re-analysed using our new approach (e.g., Nowacki *et al.* 2010; Creasy *et al.* 2017; Pisconti *et al.* 2019). We suggest that it would be worth remeasuring splitting if an S wave source side delay time > 0.5 s has been corrected for. However, for cases in which the strength of receiver and source side anisotropy was low and a sufficiently large number of measurements were made for a given path (e.g., Wookey *et al.* 2005), previous results obtained with the traditional method should generally be reliable (Fig. 10b), although it may be worth revisiting some previous studies in individual areas. Again, the traditional S-ScS differential splitting method gives more reliable results if the initial *S*-wave polarization leaving the source is close to SH (Fig. S4), so this is an important factor.

An additional complication in differential S-ScS splitting studies, even in cases in which non-horizontal propagation and the phase shift at the CMB are explicitly accounted for, has been illuminated by our modelling; this relates to the fact that the interpretation of apparent lowermost mantle splitting parameters in terms of anisotropic geometry is not straightforward. To illustrate this, we consider a uniform anisotropic patch in the lowermost mantle that is sampled by a ScS phase. The ScS phase will first experience splitting on the source side leg of the raypath through D''. Due to the sampling of the anisotropy from a different direction, even for a uniformly anisotropic D'', the splitting accumulated on the second (receiver side) leg of the raypath will be different from the source side leg. This means that the apparent D'' splitting parameters determined by S-ScS differential splitting should be regarded as a combination of two anisotropic layers, corresponding to the two legs of the raypath, with the radial component of the shear wave experiencing a phase shift in between the two legs. While previous authors have certainly been aware of this potential complication (e.g., Wookey *et al.* 2005; Nowacki *et al.* 2010; Wolf *et al.* 2019), it has generally not been explicitly taken into account in the interpretation of S-ScS differential splitting measurements. We suggest that with our improving understanding of ScS wave behaviour in anisotropic media, and the increasing sophistication of modelling tools that can explicitly account for multiple legs of the ScS path, the time is right for lowermost mantle splitting studies that use ScS phases to move beyond the horizontal raypath approximation. While ray-theoretical modelling tools can handle multiple layers of anisotropy, it is not

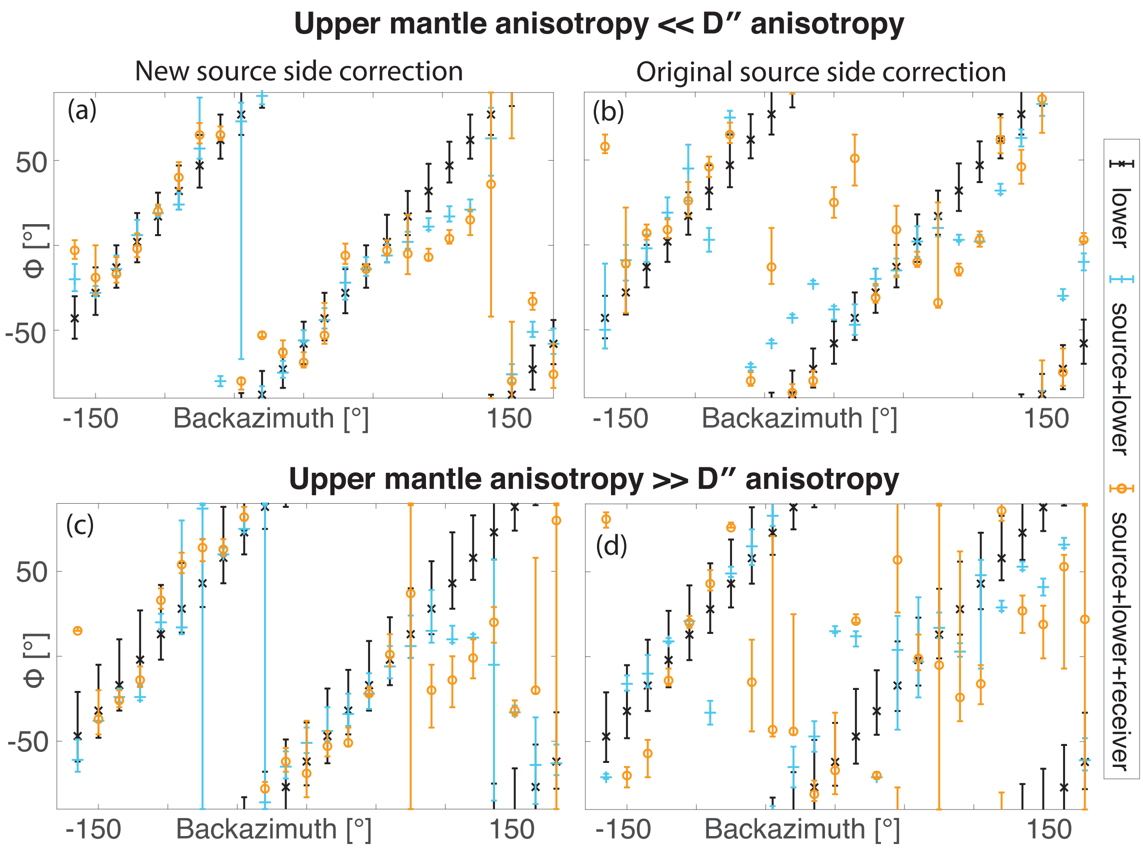

Figure 10. Demonstration of the influence of the relative strength of upper mantle compared to D'' anisotropy on the accuracy of the corrections for our newly updated (a, c) and the traditional (b, d) S-ScS differential splitting method. Results for relatively weak upper mantle anisotropy are shown in panels (a and b) and for a relatively strong upper mantle anisotropy in panels (c and d). Plotting conventions are the same as in Figs 8 and 9. The source–receiver distance for the simulations is 60° and the focal depth 0 km. The upper mantle is described by an olivine A-type elastic tensor.

clear how well ray-theoretical approximations perform for predictions of lowermost mantle splitting parameters. Nowacki & Wookey (2016) showed that ray-theory often fails at predicting the splitting of ScS due to lowermost mantle anisotropy for complex models, while the results of Wolf *et al.* (2022) suggest that ray theory does a generally good job predicting splitting parameters for uniformly anisotropic layers. We suggest that with the increasing availability (and, often, computational efficiency) of full wavefield modelling tools such as AxiSEM3D, which was utilized in this work, the community of seismologists working on lowermost mantle anisotropy from a body wave perspective may benefit from increasing use of full-wave approaches to forward modelling of lowermost mantle anisotropy.

4.2 Differential SKS-SKKS splitting intensity measurements

We now turn our attention to the reliability of SKS-SKKS splitting intensity discrepancies as an indicator of lowermost mantle anisotropy, taking into account the insights on the commutativity of the splitting intensity gained in Section 3.3. Full-wave effects on SKS-SKKS differential splitting were extensively analysed by Tesoniero *et al.* (2020), also using the AxiSEM3D synthetic modelling tool, with a focus on laterally homogeneous anisotropy models and without explicitly considering contributions from both lowermost and upper mantle anisotropy in the same models. Furthermore, the simulations of Tesoniero *et al.* (2020) were primarily for weak or modest splitting due to lowermost mantle anisotropy. Here, we expand on these results, and investigate the reliability of SKS-SKKS differential splitting intensity measurements for different amounts of splitting and different relative strengths of anisotropy in the upper and lowermost mantle.

We showed in Section 3.3 that *SI* is not necessarily commutative for strong splitting of SK(K)S phases (Fig. 6). Furthermore, we showed in Section 3.1 that for relatively complex upper mantle anisotropy models (e.g., A-, C- or E-type olivine fabric), there are deviations from the simplest $\sin 2\theta$ splitting intensity behaviour that is expected for HTI symmetry (Fig. 3). To investigate the implications of these findings for SKS-SKKS differential splitting studies, we first investigate to what extent SKS-SKKS differential splitting can be produced for models that only include upper mantle anisotropy, building on previous work (Lin *et al.* 2014; Tesoniero *et al.* 2020). We conduct simulations with input models that only include receiver side anisotropy, with a source–receiver distance of 120° (Fig. 1). In a first simulation we investigate an anisotropic layer with relatively small thickness (80 km) and then repeat the simulation for the same elastic tensor with a larger layer thickness (110 km, 140 km). We then measure SKS and SKKS splitting intensities (Fig. 1) and look for evidence of discrepancies due only to upper mantle anisotropy.

Results for HTI, olivine A-type and olivine C-type elastic tensors are shown in Fig. 7. Fig. S3 shows the same for olivine E-type. We show measurements of splitting intensity as a function of backazimuth, which corresponds to the direction from which the upper mantle elastic tensor is being sampled. We find that for relatively thin anisotropic layers, the more complex elastic tensors do predict some modest discrepancies (generally up to $\sim 0.1 - 0.2$ s) between SKS and SKKS phases for the same event-station pairs. This is consistent with previous findings (Lin *et al.* 2014; Tesoniero *et al.* 2020). Because only relatively large (>0.4) splitting intensity differences are typically interpreted as evidence for lowermost mantle anisotropy (e.g., Lynner & Long 2014; Long & Lynner 2015; Reiss *et al.* 2019; Tesoniero *et al.* 2020), such modest differences in SKS and SKKS splitting intensities (Figs 7a–c) would typically be defined as non-discrepant in the context of lowermost mantle anisotropy. We find, however, that for simulations with increased layer thickness, many SKS-SKKS measurements are in fact discrepant, even though no lowermost mantle anisotropy was incorporated in our input models (Figs 7d–f). We find that these discrepancies primarily occur when either SKS and/or SKKS splitting intensity values have high absolute values (that is, SI is lower than $\sim\!-1$ or larger than $\sim$1). Therefore, we suggest that the interpretation of (strongly) discrepant SKS-SKKS splitting intensities as reflecting a likely contribution to the splitting of one or both phases from the lowermost mantle should be limited to those measurements for which the absolute *SI*-values are less than $\sim$1 for both phases. This observation is also supported for simulations carried out for the olivine E-type elastic tensor (Fig. S3). For the case of strong splitting, leading to absolute *SI* values larger than 1, SKS-SKKS splitting discrepancies may still be interpreted by focusing on ϕ and δt instead of *SI*. (e.g., Asplet *et al.* 2020).

While this observation may help guide future studies, the implications for previously published SKS-SKKS splitting intensity discrepancy studies are likely not particularly worrisome, because interpretations of SKS-SKKS discrepancies usually rely on larger-scale patterns and (at least) tens of measurements (e.g., Wolf *et al.* 2019; Reiss *et al.* 2019; Lutz *et al.* 2020), so that a small number of potentially erroneous classifications will not carry much weight for the data set as a whole. For lower magnitudes of splitting, our results fully agree with Tesoniero *et al.* (2020), who showed that SKS-SKKS differential splitting intensity measurements are generally a robust method to detect an anisotropic signature from the lowermost mantle.

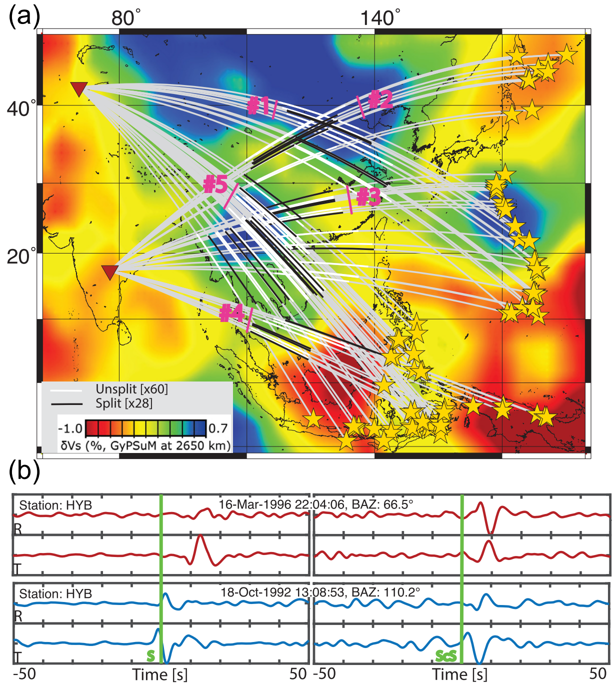

Figure 11. Illustration of our S-ScS waveform comparison technique to diagnose lowermost mantle anisotroy. (a) The two stations (AML and HYB), each of which experiences little or no splitting due to upper mantle anisotropy, are shown as red triangles, while events are shown as stars. Great circle paths between events and stations are represented by grey lines, while the portion of the ScS raypath through the lowermost 200 km of the mantle is shown in black (for those waveforms where were diagnosed as split) and white (if unsplit; see legend). Background colours indicate *S*-wave velocity perturbations from the GyPSuM tomography model (Simmons *et al.* 2010) at 2650 km depth. Five different paths with good raypath coverage are denoted in magenta. (b) Waveform examples: The transverse components of *S* and ScS for the upper example (red) have a very similar shape for *S* and ScS while a significant amount of energy has been transferred to the radial component for the ScS compared to the *S* phase, indicating splitting of the ScS wave due to of D'' anisotropy. For the lower row (blue) the transverse components of *S* and ScS look very similar while the radial flips its sign for the S compared to the ScS, indicating no splitting of the waveforms due to lowermost mantle anisotropy.

4.2.1 A new approach to diagnosing splitting due to lowermost mantle anisotropy: S-ScS waveform comparison technique

Our investigation into the effects of the phase shift at the CMB on ScS phases has illuminated potential challenges for S-ScS differential splitting measurements, but it has also pointed the way towards some improved strategies for such measurements. Specifically, we show in Sections 3.2 and 4.1 that for the ScS phase, all SH energy will be reflected at the CMB, while a small amount of SV energy may be lost (that is, transmitted into the outer core). Furthermore, the transverse component waveform (SH) will preserve its pulse shape, while the radial component waveform (SV) will undergo a phase shift that can be approximated with a change of sign (Figs 4 and 5). While this complication can lead to inaccurate source side corrections for the S-ScS differential splitting technique if not explicitly accounted for, we can also make use of it to diagnose lowermost mantle anisotropy in real data. Here we suggest a strategy for waveform comparisons of S and ScS phases that can be used to unequivocally identify a contribution to waveform behaviour from anisotropy in the lowermost mantle, and illustrate it using real data from earthquakes in the western Pacific and stations in south and central Asia.

We choose two stations (HYB and AML) in south and central Asia (red triangles in Fig. 7a), for which previous work has shown that the splitting due to upper mantle anisotropy is weak or nonexistent (Walpole *et al.* 2014). We analyse waves from earthquakes (yellow stars) from the East Asian subduction zones that occurred in a distance range between 56° and 72° from our stations. For the analysis, we compare the waveforms of S and ScS phases for the same source–receiver pair in a radial-transverse coordinate system (Fig. 7b). Based on our previous simulations, we suggest that for waveforms in which (1) the transverse components of the S and ScS phases have similar pulse shapes, (2) the radial component waveforms have similar shapes but opposite sign and (3) the radial-transverse amplitude ratio is (nearly) the same for both phases, we can reasonably infer that the S and ScS phases have sampled similar anisotropy along the raypath (Fig. 11b, lower panel). Because the raypaths of S and ScS are very similar in the upper mantle and only the ScS samples the lowermost mantle, this means that there is likely no effect on the waveform shapes from lowermost mantle anisotropy. Using a similar line of argument, if the transverse components of S and ScS have the same shape but a significantly different amount of energy arrives on the radial component for ScS compared to the S phase (Fig. 11b, upper panel), then we can infer that the ScS waveforms have been altered due to splitting (with energy being partitioned differently between the radial and transverse components) and the ScS phase has likely sampled lowermost mantle anisotropy. While this waveform comparison technique relies on visual inspection as a qualitative indicator of likely contributions from lowermost mantle anisotropy, future studies that rely on more quantitative measures of waveform similarity (e.g., via cross-correlation) may also be useful. Our waveform comparison method relies on two assumptions: first, that the splitting experienced by S and ScS due to anisotropy in the upper mantle near the source is comparable due to the similar raypath. This assumption has been explicitly tested in our study (Section 4.1) and shown to hold for most raypath geometries and reasonable upper mantle elastic tensors. Secondly, we assume that the initial polarization of the S and ScS phases are similar; given that these polarizations are controlled by the earthquake focal mechanism, and that the takeoff angles of the phases near the source are similar, this should generally hold. The assumption that the initial polarization is similar for both phases can be tested for real data in two different ways: If the focal mechanism is precisely known, the initial polarization of both phases can be calculated. An alternative approach (that is straightforward to implement for real data) is to measure the angle of the long axis of the particle motion ellipse of S and ScS. Because the radial ScS approximately flips its sign due to the CMB reflection, this angle should be $-x$ for ScS if it is x for S in a ray-centred coordinate frame (with the angle measured with respect to the backazimuth). We conduct the latter quality check in our analysis.

Another consideration for this analysis is the fact that especially at the lower end of the distance range for which we analyse events, the radial component amplitude for ScS will be lower than that for the *S* phase (in absence of lowermost mantle anisotropy), because the real part of the reflection coefficient will have an absolute values smaller than 1 (Fig. 5). For this reason, we only define a measurement as split if a relatively large energy redistribution between the radial and transverse components of the *S* and ScS phases occurs.

We apply our strategy for visual comparisons of S-ScS waveform shapes to diagnose contributions to splitting from the lowermost mantle for the data set shown in Fig. 11. Here we show great circle raypaths in grey; the portion of the ScS raypath length that traverses the lowermost 200 km of the mantle is shown in white for ScS arrivals for which no contribution to splitting from the lowermost mantle can be detected, and black for ScS waves for which we infer a contribution from the lowermost mantle. We identify five different sets of geographically similar paths with relatively dense sampling (labeled in Fig. 11), allowing us to characterize splitting in specific regions. The full data set consists of 88 S-ScS pairs; of these, 60 are non-split (with no contribution from splitting in the lowermost mantle) and 28 are split. Furthermore, we observe some relatively small-scale variability in splitting behaviour along each of the five raypaths, suggesting that lowermost mantle anisotropy may be complex and laterally varying. We illustrate our approach by showing all the waveforms for path #2 in Fig. 12. For this raypath, four ScS arrivals have been categorized as split (red coloured seismograms in Fig. 12), and the same number of ScS arrivals has been found to be non-split. For the four other paths, the full set waveforms and categorizations can be found in Figs S10–S13.

The data set shown in Fig. 11 demonstrates that there is widespread evidence for some effect of lowermost mantle anisotropy on ScS waveforms that sample the lowermost mantle beneath east Asia. We find evidence for some split waveforms along each of the five paths for which we have good sampling, although we observe a mix of split and non-split waveforms along each. This mix of split and non-split behaviour may reflect differences in initial polarizations of the ScS phases, with some waveforms being initially polarized along a fast or slow direction of the anisotropic medium (which is consistent with the spread of initial polarizations from our data). Alternatively, it may reflect small-scale variations in the strength and/or geometry of seismic anisotropy at the base of the mantle. It is not trivial, however, to reconcile inferences of small-scale variability with the large Fresnel zones of ScS at the CMB which span ∼900 km laterally for a dominant period of 10 s (Nowacki 2013). While visual inspection of ScS waveforms provides a useful tool for diagnosing the likely presence of lowermost mantle anisotropy, by itself it cannot provide specific constraints on the geometry of anisotropy. Future work that applies a range of different analysis techniques, and examines a range of seismic phases (e.g., Creasy *et al.* 2021), to study lowermost mantle anisotropy beneath this study region will be needed to fully elucidate the anisotropic geometry.

While the waveform examination technique we discuss here provides a useful and straightforward mechanism for diagnosing the effect of lowermost anisotropy on ScS waveforms, it has some significant limitations. As discussed above, by itself it cannot provide specific constraints on the geometry of anisotropy, just its likely presence. It may therefore be particularly well suited as a tool for initial or preliminary surveys of different regions of the lowermost mantle, which can then be followed up with more detailed studies that use a range of measurement techniques (including the improved S-ScS differential splitting algorithm and SKS-SKKS splitting intensity discrepancy strategies discussed in this paper). A second disadvantage of this technique is that it can only be applied at stations that exhibit little or no splitting due to upper mantle anisotropy at the frequencies of interest, limiting its applicability. On the other hand, when a null station has been identified, a large amount of ScS data can be efficiently processed using this technique; because the details of the waveforms are less important than the energy distribution between radial and transverse, a larger number of waveforms may be able to be used than in traditional S-ScS differential splitting studies. We suggest that the waveform comparison technique may be able to be routinely applied as an initial step in studies of lowermost mantle anisotropy using body waves as reliable diagnostic indicator of the presence of anisotropy, before applying other measurement methods as a follow-up.

5 CONCLUSION

In this work, we have explored the assumptions commonly made in studies of deep mantle anisotropy using shear wave splitting via global wavefield simulations using AxiSEM3D. We have focused particularly on the accuracy of explicit corrections for splitting due to anisotropy elsewhere along the raypath (typically in the upper mantle, on either the source or receiver side). We have shown that corrections for upper mantle anisotropy can generally be applied successfully, but the accuracy of the corrections depends on the strength of upper mantle anisotropy and on its geometry, with more complex (but perhaps more realistic) elasticity scenarios introducing some inaccuracy in the corrections. We have shown that the

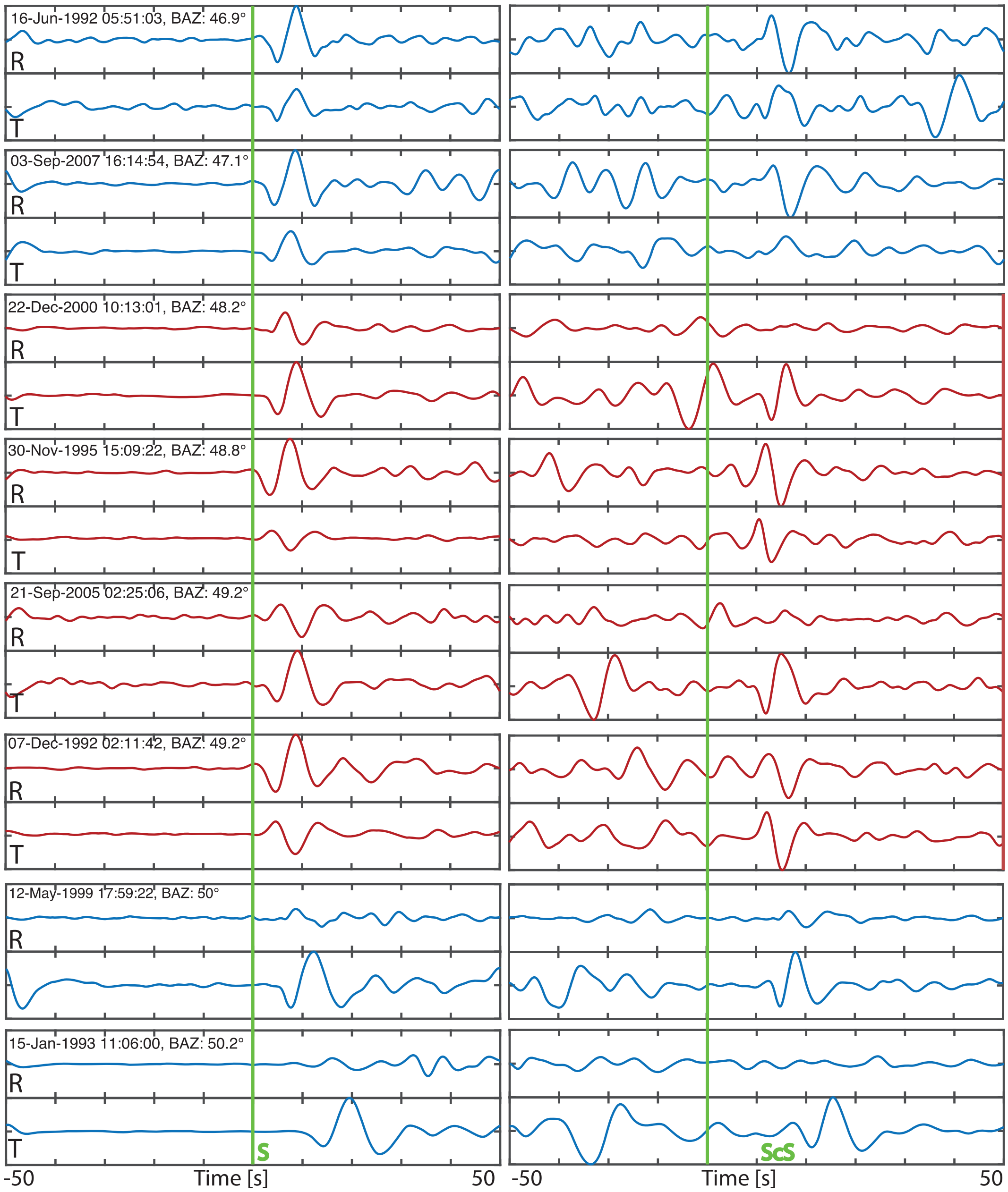

Figure 12. Radial (R) and transverse (T) waveforms for path #2 of Fig. 11, ordered with increasing backazimuth from top to bottom. *S* waveforms are shown to the left and ScS waveforms to the right. Predicted phase arrivals (for the PREM velocity model) are indicated by green lines. Split S-ScS pairs are shown in red colour and non-split pairs in blue colour.

traditional S-ScS differential splitting technique, which relies on an approximation that the ScS raypath is horizontal in the lowermost mantle and does not explicitly account for the reflection at the CMB, can introduce inaccurate corrections for the effect of splitting due to anisotropy in the source side upper mantle. The degree of the inaccuracy of the correction will depend on the strength of the upper mantle splitting (relative to that due to lowermost mantle anisotropy) and on the initial polarization of the wave (with waves that have more SV energy being more strongly affected). We have proposed an updated algorithm for S-ScS differential splitting that explicitly takes into account the phase shift at the CMB due to the reflection and tested it with a suite of synthetic models. We have also interrogated the assumptions in the SKS-SKKS differential splitting intensity method and have shown that for strong cumulative splitting, the assumption that the splitting intensity is commutative breaks down. We have found that SKS-SKKS differential splitting intensity measurements are generally a viable tool to resolve lowermost mantle anisotropy, but the method should only be used for splitting intensity values with an absolute value of less than 1 s for both phases. We have proposed a new waveform comparison technique for S-ScS phases to diagnose the presence of lowermost mantle anisotropy and applied it to East Asia. We have shown that interpreting S-ScS differential splitting and differential SKS-SKKS splitting intensities in terms of lowermost mantle anisotropy is most reliable for stations which overly isotropic or only weakly anisotropic upper mantle and crust. This implies that for the reliable analysis of deep mantle anisotropy such stations should be preferably selected. Stations that are known to exhibit null splitting (no upper mantle contribution) are an excellent choice since both, the S-ScS waveform comparison technique and the S-ScS differential splitting technique can be applied to the same data set.

The insights gained from our synthetic modelling should help to make estimates of splitting due to deep mantle anisotropy more accurate going forward. Furthermore, our work helps to illustrate the promise of synthetic waveform modelling using global wavefield simulation tools that are capable of handling arbitrary anisotropy, such as AxiSEM3D, in understanding the geometry of anisotropy in the deep mantle. Ultimately, such approaches will enhance our ability to infer flow directions in deep mantle settings, including the deep upper mantle beneath subducting slabs, the mantle transition zone, and the D'' layer at the base of the mantle, opening up new avenues for understanding the dynamics and processes of the deep Earth.

ACKNOWLEDGMENTS

This work was funded by Yale University and by the National Science Foundation (USA) via grant EAR-1547499 to MDL. KL and TNM acknowledge support from NERC Grant NE/R012199/1. We gratefully acknowledge the Yale Center for Research Computing for guidance and use of the research computing infrastructure, specifically the Grace cluster. The Generic Mapping Tools (Wessel & Smith 1998), ObsPy (Beyreuther *et al.* 2010), MSAT (Walker & Wookey 2012) and SplitRacer (Reiss & Rümpker 2017) were used in this research. We are grateful to the editor Ana Ferreira and two anonymous reviewers for constructive comments.

DATA AVAILABILITY

All synthetic seismograms for this study were computed using AxiSEM3D, which is publicly available at https://github.com/kuangdai/AxiSEM-3D.

REFERENCES

Asplet, J., Wookey, J. & Kendall, M., 2020. A potential post-perovskite province in D" beneath the Eastern Pacific: evidence from new analysis of discrepant SKS–SKKS shear-wave splitting, *Geophys. J. Int.,* **221,** 2075–2090.

Barruol, G. & Kern, H., 1996. Seismic anisotropy and shear-wave splitting in lower-crustal and upper-mantle rocks from the Ivrea Zone: experimental and calculated data, *Phys. Earth planet. Inter.,* **95,** 175–194.

Barruol, G., Wuestefeld, A. & Bokelmann, G., 2009. SKS-Splitting-database, Université de Montpellier, Laboratoire Géosciences.

Beyreuther, M., Barsch, R., Krischer, L., Megies, T., Behr, Y. & Wassermann, J., 2010. Obspy: a python toolbox for seismology, *Seismol. Res. Lett.,* **81,** 530–533.

Bowman, J.R. & Ando, M., 1987. Shear-wave splitting in the upper-mantle wedge above the Tonga subduction zone, *Geophys. J. R. astr. Soc.,* **88,** 25–41.

Chang, S.-J. & Ferreira, A. M.G., 2019. Inference on water content in the mantle transition zone near subducted slabs from anisotropy Tomography, *Geochem. Geophys. Geosyst.,* **20,** 1189–1201.

Chang, S.-J., Ferreira, A. M.G., Ritsema, J., van Heijst, H.J. & Woodhouse, J.H., 2015. Joint inversion for global isotropic and radially anisotropic mantle structure including crustal thickness perturbations, *J. geophys. Res.,* **120**(6), 4278–4300.

Chang, S.-J., Ferreira, A.M.G., Ritsema, J., van Heijst, H.J. & Woodhouse, J.H., 2014. Global radially anisotropic mantle structure from multiple datasets: a review, current challenges, and outlook, *Tectonophysics,* **617,** 1–19.

Chapman, C., 2004. *Fundamentals of Seismic Wave Propagation,* Cambridge Univ. Press.

Chevrot, S., 2000. Multichannel analysis of shear wave splitting, *J. geophys. Res.,* **105,** 21 579–21 590.

Chevrot, S., 2006. Finite-frequency vectorial tomography: a new method for high-resolution imaging of upper mantle anisotropy, *Geophys. J. Int.,* **165,** 641–657.

Cottaar, S. & Romanowicz, B., 2013. Observations of changing anisotropy across the southern margin of the African LLSVP, *Geophys. J. Int.,* **195,** 1184–1195.

Creasy, N., Long, M.D. & Ford, H.A., 2017. Deformation in the lowermost mantle beneath Australia from observations and models of seismic anisotropy, *J. geophys. Res.,* **122,** 5243–5267.

Creasy, N., Miyagi, L. & Long, M.D., 2020. A library of elastic tensors for lowermost mantle seismic anisotropy studies and comparison with seismic observations, *Geochem. Geophys. Geosyst.,* **21,** e2019GC008883.

Creasy, N., Pisconti, A., Long, M.D. & Thomas, C., 2021. Modeling of seismic anisotropy observations reveals plausible lowermost mantle flow directions beneath Siberia, *Geochem. Geophys. Geosyst.,* **22**(10), e2021GC009924.

Davaille, A. & Romanowicz, B., 2020. Deflating the LLSVPs: bundles of mantle thermochemical plumes rather than thick stagnant "Piles", *Tectonics,* **39**(10).

Deng, J., Long, M.D., Creasy, N., Wagner, L., Beck, S., Zandt, G., Tavera, H. & Minaya, E., 2017. Lowermost mantle anisotropy near the eastern edge of the Pacific LLSVP: constraints from SKS-SKKS splitting intensity measurements, *Geophys. J. Int.,* **210,** 774–786.

Dziewonski, A.M. & Anderson, D.L., 1981. Preliminary reference earth model, *Phys. Earth planet. Inter.,* **25,** 297–356.

Dziewonski, A.M., Lekic, V. & Romanowicz, B.A., 2010. Mantle anchor structure: an argument for bottom up tectonics, *Earth planet. Sci. Lett.,* **299,** 69–79.

Eakin, C., Rychert, C. & Harmon, N., 2018. The role of oceanic transform faults in seafloor spreading: a global perspective from seismic anisotropy, *J. geophys. Res.,* **123,** 1736–1751.

Eakin, C.M. & Long, M.D., 2013. Complex anisotropy beneath the Peruvian flat slab from frequency-dependent, multiple-phase shear wave splitting analysis, *J. geophys. Res.,* **118,** 4794–4813.

Erdman, M.E., Hacker, B.R., Zandt, G. & Seward, G., 2013. Seismic anisotropy of the crust: electron-backscatter diffraction measurements from the Basin and Range, *Geophys. J. Int.,* **195,** 1211–1229.

Faccenda, M., 2014. Mid mantle seismic anisotropy around subduction zones, *Phys. Earth planet. Inter.,* **227,** 1–19.

Ferreira, A. M.G., Woodhouse, J.H., Visser, K. & Trampert, J., 2010. On the robustness of global radially anisotropic surface wave tomography, *J. geophys. Res.,* **115**(B4).

Ferreira, A., Faccenda, M., Sturgeon, W., Chang, S.-J. & Schardong, L., 2019. Ubiquitous lower-mantle anisotropy beneath subduction zones, Nature Geoscience, **12,** 301–306.

Foley, B.J. & Long, M.D., 2011. Upper and mid-mantle anisotropy beneath the Tonga slab, *Geophys. Res. Lett.,* **38**.

Ford, H.A., Long, M.D., He, X. & Lynner, C., 2015. Lowermost mantle flow at the eastern edge of the African large low shear velocity province, *Earth planet. Sci. Lett.,* **420,** 12–22.

Fry, B., Deschamps, F., Kissling, E., Stehly, L. & Giardini, D., 2010. Layered azimuthal anisotropy of Rayleigh wave phase velocities in the European Alpine lithosphere inferred from ambient noise, *Earth planet. Sci. Lett.,* **297**(1), 95–102.

Garnero, E.J., Moore, M.M., Lay, T. & Fouch, M.J., 2004. Isotropy or weak vertical transverse isotropy in D" beneath the Atlantic Ocean, *J. geophys. Res.,* **109**(B8), 1–10.

Grund, M. & Ritter, J.R., 2018. Widespread seismic anisotropy in Earth's lowermost mantle beneath the Atlantic and Siberia, *Geology,* **47,** 123–126.

Hernlund, J., Thomas, C. & Tackley, P., 2005. A doubling of the post-perovskite phase boundary and structure of the Earth's lowermost mantle, *Nature,* **434,** 882–886.

Karato, S.-I., Jung, H., Katayama, I. & Skemer, P., 2008. Geodynamic significance of seismic anisotropy of the upper mantle: new insights from laboratory studies, *Ann. Rev. Earth planet. Sci.,* **36,** 59–95.

Kneller, E.A., van Keken, P.E., ichiro Karato, S. & Park, J., 2005. B-type olivine fabric in the mantle wedge: Insights from high-resolution non-newtonian subduction zone models, *Earth planet. Sci. Lett.,* **237,** 781–797.

Kustowski, B., Ekström, G. & Dziewoński, A.M., 2008. Anisotropic shear-wave velocity structure of the Earth's mantle: a global model, *J. geophys. Res.,* **113**(B6), doi:10.1029/2007JB005169.

Leng, K., Nissen-Meyer, T. & van Driel, M., 2016. Efficient global wave propagation adapted to 3-D structural complexity: a pseudospectral/spectral-element approach, *Geophys. J. Int.,* **207**(3), 1700–1721.

Leng, K., Nissen-Meyer, T., van Driel, M., Hosseini, K. & Al-Attar, D., 2019. AxiSEM3D: broad-band seismic wavefields in 3-D global earth models with undulating discontinuities, *Geophys. J. Int.,* **217**(3), 2125–2146.

Levin, V. & Park, J., 1997. P-SH conversions in a flat-layered medium with anisotropy of arbitrary orientation, *Geophys. J. Int.,* **131**(2), 253–266.

Lin, Y.-P., Zhao, L. & Hung, S.-H., 2014. Full-wave effects on shear wave splitting, *Geophys. Res. Lett.,* **41,** 799–804.

Long, M., 2009. Complex anisotropy in D" beneath the eastern Pacific from SKS-SKKS splitting discrepancies, *Earth planet. Sci. Lett.,* **283,** 181–189.

Long, M.D. & Becker, T., 2010. Mantle dynamics and seismic anisotropy, *Earth planet. Sci. Lett.,* **297,** 341–354.

Long, M.D. & Lynner, C., 2015. Seismic anisotropy in the lowermost mantle near the Perm Anomaly, *Geophys. Res. Lett.,* **42,** 7073–7080.

Lutz, K., Long, M., Creasy, N. & Deng, J., 2020. Seismic anisotropy in the lowermost mantle beneath North America from SKS-SKKS splitting intensity discrepancies, *Phys. Earth planet. Inter.,* **305,** 106504.

Lynner, C. & Long, M.D., 2012. Evaluating contributions to SK(K)S splitting from lower mantle anisotropy: a case study from station DBIC, cote D'Ivoire, *Bull. seism. Soc. Am.,* **102,** 1030–1040.

Lynner, C. & Long, M.D., 2013. Sub-slab seismic anisotropy and mantle flow beneath the Caribbean and Scotia subduction zones: effects of slab morphology and kinematics, *Earth planet. Sci. Lett.,* **361,** 367–378.

Lynner, C. & Long, M.D., 2014. Lowermost mantle anisotropy and deformation along the boundary of the African LLSVP, *Geophys. Res. Lett.,* 3447–3454.

Lynner, C. & Long, M.D., 2015. Heterogeneous seismic anisotropy in the transition zone and uppermost lower mantle: evidence from South America, Izu-Bonin and Japan, *Geophys. J. Int.,* **201,** 1545–1552.

Mohiuddin, A., Long, M.D. & Lynner, C., 2015. Mid-mantle seismic anisotropy beneath Southwestern Pacific subduction systems and implications for mid-mantle deformation, *Phys. Earth planet. Inter.,* **245**.

Nikulin, A., Levin, V. & Park, J., 2009. Receiver function study of the Cascadia megathrust: evidence for localized serpentinization, *Geochem. Geophys. Geosyst.,* **10**(7).

Niu, F. & Perez, A.M., 2004. Seismic anisotropy in the lower mantle: a comparison of waveform splitting of SKS and SKKS, *Geophys. Res. Lett.,* **31**(24).

Nowacki, A., 2013. *Plate Deformation from Cradle to Grave: Seismic Anisotropy and Deformation at Mid-Ocean Ridges and in the Lowermost Mantle,* Springer.

Nowacki, A. & Wookey, J., 2016. The limits of ray theory when measuring shear wave splitting in the lowermost mantle with ScS waves, *Geophys. J. Int.,* **207,** 1573–1583.

Nowacki, A., Wookey, J. & Kendall, J.-M., 2010. Deformation of the lowermost mantle from seismic anisotropy, *Nature,* **467,** 1091–1094.

Nowacki, A., Wookey, J. & Kendall, J.-M., 2011. New advances in using seismic anisotropy, mineral physics and geodynamics to understand deformation in the lowermost mantle, *J. Geodyn.,* **52,** 205–228.

Panning, M.P. & Nolet, G., 2008. Surface wave tomography for azimuthal anisotropy in a strongly reduced parameter space, *Geophys. J. Int.,* **174**(2), 629–648.

Panning, M.P. & Romanowicz, B., 2006. A three-dimensional radially anisotropic model of shear velocity in the whole mantle, *Geophys. J. Int.,* **167,** 361–379.

Parisi, L., Ferreira, A. M.G. & Ritsema, J., 2018. Apparent splitting of s waves propagating through an isotropic lowermost mantle, *J. geophys. Res.,* **123,** 3909–3922.

Pisconti, A., Thomas, C. & Wookey, J., 2019. Discriminating between causes of D" anisotropy using reflections and splitting measurements for a single path, *J. geophys. Res.,* **124**(5), 4811–4830.

Reiss, M.C., Long, M.D. & Creasy, N., 2019. Lowermost mantle anisotropy beneath Africa from differential SKS-SKKS shear-wave splitting, *J. geophys. Res.,* **124**(8), 8540–8564.

Reiss, M.C. & Rümpker, G., 2017. SplitRacer: MATLAB code and GUI for semiautomated analysis and interpretation of teleseismic shear-wave splitting, *Seismol. Res. Lett.,* **88,** 392–409.

M.Russo, R., Gallego, A., Comte, D., Mocanu, V., Murdie, R. & VanDecar, J., 2010. Source-side shear wave splitting and upper mantle flow in the Chile ridge subduction region, *Geology,* **38,** 707–710.

Russo, R.M. & Silver, P.G., 1994. Trench-parallel flow beneath the Nazca plate from seismic anisotropy, **263**(5150), 1105–1111.

Schulte-Pelkum, V., Monsalve, G., Sheehan, A., Pandey, M., Sapkota, S., Bilham, R. & Wu, F., 2005. Imaging the Indian subcontinent beneath the Himalaya, *Nature,* **435,** 1222–1225.

Silver, P.G., 1996. Seismic anisotropy beneath the continents: probing the depths of geology, annual review of earth and planetary sciences, **24**(1), 385–432.

Silver, P.G. & Chan, W.W., 1991. Shear wave splitting and subcontinental mantle deformation, *J. geophys. Res.,* **96,** 16 429–16 454.

Silver, P.G. & Long, M.D., 2011. The non-commutivity of shear wave splitting operators at low frequencies and implications for anisotropy tomography, *Geophys. J. Int.,* **184**(3), 1415–1427.

Simmons, N.A., Forte, A.M., Boschi, L. & Grand, S.P., 2010. GyPSuM: a joint tomographic model of mantle density and seismic wave speeds, *J. geophys. Res.,* **115**(B12),

Tesoniero, A., Leng, K., Long, M.D. & Nissen-Meyer, T., 2020. Full wave sensitivity of SK(K)S phases to arbitrary anisotropy in the upper and lower mantle, *Geophys. J. Int.,* **222**(1), 412–435.

Vinnik, L., Farra, V. & Romanowicz, B., 1989. Azimuthal anisotropy in the earth from observations of SKS at GEOSCOPE and NARS broadband stations, *Bull. seism. Soc. Am.,* **79,** 1542–1558.

Walker, A. & Wookey, J., 2012. MSAT - a new toolkit for the analysis of elastic and seismic anisotropy, *Comp. Geosci.,* **49,** 81–90.

Walpole, J., Wookey, J., Kendall, J.-M. & Masters, T.-G., 2017. Seismic anisotropy and mantle flow below subducting slabs, *Earth planet. Sci. Lett.,* **465,** 155–167.

Walpole, J., Wookey, J., Masters, G. & Kendall, J.M., 2014. A uniformly processed data set of SKS shear wave splitting measurements: a global investigation of upper mantle anisotropy beneath seismic stations, *Geochem. Geophys. Geosyst.,* **15,** 1991–2010.

Walsh, E., Arnold, R. & Savage, M.K., 2013. Silver and Chan revisited, *J. geophys. Res.,* **118,** 5500–5515.

Wang, Y. & Wen, L., 2004. Mapping the geometry and geographic distribution of a very low velocity province at the base of the Earth's mantle, *J. geophys. Res.,* **109**(10),

Wessel, P. & Smith, W. H.F., 1998. New, improved version of generic mapping tools released, *EOS, Trans. Am. Geophys. Un.,* **79,** 579–579.

Wirth, E.A. & Long, M.D., 2012. Multiple layers of seismic anisotropy and a low-velocity region in the mantle wedge beneath Japan: evidence from teleseismic receiver functions, *Geochem. Geophys. Geosyst.,* **13**(8).

Wolf, J., Creasy, N., Pisconti, A., Long, M.D. & Thomas, C., 2019. An investigation of seismic anisotropy in the lowermost mantle beneath Iceland, *Geophys. J. Int.,* **219**(Suppl. 1), S152–S166.

Wolf, J. & Evans, D.A.D. 2022. Reconciling supercontinent cycle models with ancient subduction zones, *Earth planet. Sci. Lett.,* **578,**117293.

Wolf, J., Long, M.D., Leng, K. & Nissen-Meyer, T., 2022. Sensitivity of SK(K)S and ScS phases to heterogeneous anisotropy in the lowermost mantle from global wavefield simulations, *Geophys. J. Int.,* **228,** 366–386.

Wookey, J. & Kendall, J.-M., 2008. Constraints on lowermost mantle mineralogy and fabric beneath Siberia from seismic anisotropy, *Earth planet. Sci. Lett.,* **275,** 32–42.

Wookey, J., Kendall, J.-M. & Rümpker, G., 2005. Lowermost mantle anisotropy beneath the north Pacific from differential S-ScS splitting, *Geophys. J. Int.,* **161,** 829–838.

Yuan, K. & Beghein, C., 2014. Three-dimensional variations in Love and Rayleigh wave azimuthal anisotropy for the upper 800km of the mantle, *J. geophys. Res.,* **119,** 3232–3255.

SUPPORTING INFORMATION

Supplementary data are available at *GJI* online.

Figure S1. Test how accurate receiver side anisotropy corrections are for an olivine E-type upper mantle. (a) Analysis of receiver-side splitting parameters measuring *SI* as a function of backazimuth for SKS phases. Orange circles indicate splitting measurements with the error bars showing 95 per cent confidence regions determined using SplitRacer. Upper mantle splitting parameters are noted in the subplots. (b–c) Delay times (b) and fast polarization directions (c) associated with source side anisotropy determined using *S* phases as schematically shown in Fig. 2b of the main manuscript. Black circles show measurement values for simulations for which only source side anisotropy is incorporated into the input models. Blue signs show values after receiver side correction for simulations that use input models with source side and receiver side anisotropy (legend). 95 per cent confidence intervals are again shown by error bars. The receiver side splitting parameters used for the correction are those shown in panel (a). This figure is like Fig. 3 of the main manuscript, just for E-type olivine in the upper mantle.

Figure S2. Splitting parameters. (upper row) and δt (lower row) as a function of backazimuth for the simulations shown in Fig. 6 of the main manuscript. The splitting is measured from synthetic waveforms derived from simulations with different strengths of splitting due to upper mantle anisotropy (assuming A-type olivine) for a source–receiver distance of 60°. The splitting intensity is measured as a function of backazimuth from S phases for simulations that only include source side anisotropy (grey) and source+receiver side anisotropy (black), with the error bars indicating 95 per cent confidence intervals. The backazimuth corresponds to the direction from which the elastic tensor is sampled. By design, the seismic anisotropy that the seismic wave samples on source and receiver side is identical. Measurements were conducted for a low (left-hand column), medium (middle column) and large (right-hand column) strength of anisotropy. In general, δt values are observed to be twice as large when sampling source+receiver side anisotropy compared to only sampling receiver side anisotropy, while. values are largely independent of the sampled integrated strength of anisotropy.

Figure S3. Splitting intensity measurements for SK(K)S phases in the presence of only upper mantle anisotropy for an epicentral distance of 120°. The results are shown as a function of backazimuth, which corresponds to the direction from which the elastic tensor is sampled. Black dashed lines indicate splitting intensity values of 1 and −1. Black circles indicate SKS and blue circles SKKS splitting intensities, with error bars showing 95 per cent confidence intervals. Results are for (a) moderate upper mantle splitting (layer thickness of 120 km) (b) strong upper mantle splitting (layer thickness of 250 km). Same as Fig. 7 of the main paper for E-type olivine in the upper mantle.

Figure S4. Estimates of lowermost mantle-associated splitting parameters δt (a,c,e) and (b,d,f) for ScS phases, after correction for upper mantle anisotropy, for models with different elastic tensors in the upper mantle: HTI (a–b), olivine A-type (c–d) and olivine C-type (e–f). All measurements are shown as a function of backazimuth, which corresponds to the direction from which the upper mantle anisotropy is sampled. We rotate the Ppv elastic tensor in the lowermost mantle in our simulations, such that it is always sampled from the same direction (and therefore the same splitting due to lowermost mantle anisotropy is expected in all simulations). The source–receiver distance for these results is 60° and the focal depth 0 km. Measurements on waveforms computed for a model with no upper mantle anisotropy (corresponding to the expected splitting signal after upper mantle corrections) are shown by black crosses. Blue plus-signs show estimated splitting parameters after correcting for the source side anisotropy implemented in the simulations in the absence of receiver side anisotropy. Yellow circles show results after applying all anisotropy corrections using the corrected S-ScS differential splitting technique for simulations that include source-, receiver side- and lowermost mantle anisotropy. In each case error bars indicate 95 per cent confidence regions. We find that, δt determined by the corrected S-ScS differential splitting technique is generally less reliable, while ϕ. is more robust. This figure is like Fig. 8 of the main manuscript, but here for an initially SH-polarized wave.

Figure S5. Like Fig. S4, the only differences are the purely SV initial source polarization for *S* and ScS and the lowermost mantle elastic tensor, which is bridgmanite (Br).

Figure S6. Lowermost mantle associated splitting parameters δt (a, c) and. (b, d) for an olivine E-type elastic tensor with an initial source polarization of *S* and ScS of pure SV (a–b) and pure SH (c–d). The initial The lowermost mantle elastic tensor is post-perovskite (Ppv). The source–receiver distance for these results is 60° and the focal depth 0 km. The plotting conventions are as in Figs S4 and S5.

Figure S7. Like Fig. S4, the only differences are the purely SV initial source polarization for S and ScS and a focal depth of 500 km (and thus deeper source-side anisotropy).

Figure S8. Demonstration of the influence of the relative strength of upper mantle compared to D'' anisotropy on the accuracy of the corrections for our newly updated (a, c) and the traditional (b, d) S-ScS differential splitting method. Results for relatively weak upper mantle anisotropy are shown in panels (a–b) and for a relatively strong upper mantle anisotropy in panels (c–d). Plotting conventions are the same as in Figs S10 and S11. The source–receiver distance for the simulations is 60° and the focal depth 0 km. The upper mantle is described by an olivine A-type elastic tensor. This figure is like Fig. 10 of the main manuscript for an initially SH polarized wave.

Figure S9. Demonstration of the influence of the relative strength of upper mantle compared to D'' anisotropy on the accuracy of the corrections for our newly updated (a, c) and the traditional (b, d) S-ScS differential splitting method. Results for relatively weak upper mantle anisotropy are shown in panels (a–b) and for a relatively strong upper mantle anisotropy in panels (c–d). Plotting conventions are the same as in Figs S10 and S11. The source–receiver distance for the simulations is 60° and the focal depth 0 km. The upper mantle is described by an olivine A-type elastic tensor. This figure is like is for the same simulations as from Fig. 10 of the main manuscript but shows the results for δt.

Figure S10. Radial (*R*) and transverse (*T*) waveforms for path #1 of Fig. 12, ordered with increasing backazimuth from top to bottom. *S* waveforms are shown to the left and ScS waveforms to the right. Predicted phase arrivals (for the PREM velocity model) are indicated by green lines. Split S-ScS pairs are shown in red colour and non-split pairs in blue colour.

Figure S11. Like Fig. S10 for path #3.

Figure S12. Like Fig. S10 for path #4.

Figure S13. Like Fig. S10 for path #5.